ORIGINAL ARTICLE

Facile and green synthesis of CuS-activated carbon nanocomposite from *Sargassum siliquastrum* biomass for fast and efficient removal of eosin yellow dye

Ibrahem M. A. Hasan[1] · Fawzy H. Assaf[1] · Ahmed R. Tawfik[1]

Abstract

Sargassum spp. comprise significant amounts of biomass which can be risky for environmental and economic activities; thus, taking the advantage of this underutilized raw material could make a significant contribution to long-term sustainability. In this study, *Sargassum siliquastrum* (*SS*) brown alga was successfully transformed into CuS nanoparticles–activated carbon (CuS NPs–AC) composite for adsorption of the hazardous dye eosin yellow (EY) from aqueous solutions. The CuS NPs–AC sorbent was characterized through FTIR, XRD, SEM-EDX, and S_{BET} analyses. Characterization results revealed the successful formation of CuS NPs–AC nanocomposite. Results of the adsorption process indicated that EY was efficiently removed with a percentage of 99.6% at the optimum conditions; pH 7, 120 min contact time, 2 g/L CuS NPs–AC dose, and 300 mg/L initial EY concentration. Adsorption data fitted well with pseudo-second-order kinetics and Langmuir isotherm model with a monolayer adsorption capacity of 303.03 mg/g at 328 K. Thermodynamic analyses revealed that the adsorption process was spontaneous and endothermic. The adsorbent showed high selectivity towards EY and followed a three-stage intraparticle diffusion mechanism. The potent adsorption of EY by CuS NPs–AC nanocomposite was attributed to electrostatic attraction, π-π stacking, halogen bonding, and hydrogen bonding. This study developed a reliable and cost-effective adsorbent for removing EY dye from water.

Keywords Activated carbon · Adsorption · CuS NPs · Eosin yellow · *Sargassum siliquastrum*

Highlights

• The brown alga *Sargassum siliquastrum* was utilized to prepare CuS NPs–AC nanoadsorbent for EY removal.

• The adsorbent was systematically characterized by FTIR, XRD, SEM-EDX, and BET analyses.

• A complete removal of 300 mg/L EY was achieved within 120 min by 2 g/L dosage under neutral conditions.

• The experimental data fitted well with Langmuir model with maximum adsorption capacity of 303.03 mg/g.

• The low-cost and eco-friendly adsorbent can be a viable alternative to the commercial AC for water treatment.

✉ Ibrahem M. A. Hasan
  hasan111167@gmail.com

✉ Ahmed R. Tawfik
  atawfik2018@gmail.com

[1] Chemistry Department, Faculty of Science, South Valley University, Qena 83523, Egypt

1 Introduction

Most dye effluents are water-soluble and discharged into rivers, streams, and other water resources. These effluents compromise our environmental shield and lead to water pollution. The presence of synthetic dyes in water poses a significant risk to the environment as they obstruct the penetration of light, hinder aquatic photosynthesis, and cause disruption to the entire ecological system. Additionally, it has been observed that the exposure to these dyes through the food chain can be highly toxic and often results in fatality for humans [1, 2]. Dye residues in soil have a negative impact on plant and animal health as well as soil fertility. These dyes must be removed from water because their complex structures make them resistant to biodegradation [3, 4].

EY, a member of the fluoresce class of anionic dyes, can be identified by its IUPAC name; 2-(2,4,5,6-tetrabromo-6-oxido-3-oxo-3H-xanthene-9-yl)benzoate disodium salt. With high solubility in water, it has the ability to strongly absorb red blood cells and imparts a red color, which makes

it useful in staining various bacterial species. However, its use in food has been prohibited by the US government due to its toxicity. [5]. EY poses significant toxicological risks including severe skin and eye irritation resulting in redness and pain. It can also has adverse effects on vital organs like liver and kidney, as well as cause serious corneal injury by destroying retinal ganglion cells. Furthermore, it can lead to alterations in the DNA of gastrointestinal organs in living organisms, potentially resulting in various diseases in humans [6].

After being broken down by heat, an oxidizing agent, and light, dyes' metabolites are also extremely toxic and have cancer-causing properties [6]. It was thought worthwhile to develop a cost-effective and quick method for removing EY from wastewater. Numerous techniques for treating wastewater have been developed over the years including electrochemical treatment [7], filtration [8], coagulation or flocculation [9], photocatalysis [10], and reverse osmosis [11]. But the majority of these techniques have shown their efficacy in the discharge of dyes at the laboratory level. In addition, they are expensive, require a lot of energy and time to operate, and occasionally produce enormous amounts of sludge that would otherwise need to be properly treated to prevent climate contamination. Thus, their use in industry has been restricted [12, 13]. Adsorption methods have become the standard for water treatment. Adsorption, as opposed to other approaches, could be seen as a promising choice for the discharge of dyes from wastewater due to its effectiveness, high selectivity, low cost, ease of use, and accessibility in a variety of trial conditions [13–17]. Utilization of low-cost, environmentally friendly, and high surface area adsorbents to increase process economy and cost effectiveness has been the focus of many efforts to date. This is why it is challenging to achieve an affordable wastewater treatment without simultaneous modeling and variable optimization [5].

Given these risks, the research community has explored a broad range of adsorbent materials focusing on hybrids and composites made of innovative materials such as carbon nanotubes (CNTs), conducting polymers, and metal/metal oxide nanoparticles [16]. Activated carbon (AC) is especially sought-after due to its unique and cost-effective properties, making it highly desirable for a wide range of applications. Generally, carbonaceous materials have lower costs and require less energy for regeneration compared to other options [18]. Moreover, the textural characteristics of AC including surface area and pore structure can be customized according to the specific application requirements [19]. Their remarkable thermal and chemical stability enables them to establish surface functional groups with numerous oxygen-containing molecules [20]. Additionally, they are great choices for separation applications because of their rapid kinetics, high potential for recycling,

and most importantly, their ability to adsorb molecules in both liquid and gaseous phases [21]. Consequently, there is a pressing need on a worldwide scale to create and develop sophisticated AC materials with exceptional capabilities for removing dyes [5]. The efficient utilization of biomass is drawing attention for the sustainable fabrication of biological chemicals and products. Biomass provides the potential for the large-scale manufacturing of porous carbon since it is an available, affordable, and viable carbon precursor. The advantages of environmental and sustainable management are currently revealed through the use of biomass such as rice husks, stems, sludge, garlic peels, corncobs, and wasted leaves [22]. One particular kind of biomass is algae that are rich in lignin, cellulose, and hemicelluloses with C, H, and O as main elements making them good raw materials for the production of carbon. Recently, the developments in synthesis techniques for porous carbon derived from algae were reviewed, and their prospective uses in energy storage, adsorption, and catalysis were discussed [22, 23].

In this context, *Sargassum* is a brown alga found in the world's oceans' tropical and subtropical waters. *Sargassum*, whether benthic or pelagic, represents significant amounts of biomass, and enormous beaching episodes, often known as "golden tides," which poses challenges for environmental and tourist managers. The biomass of *Sargassum* has the potential to provide economic benefits; however, the increasing reports of invasion in different regions worldwide and micropollutant contamination negate this wealth. Similarly, there are worries about widespread use or disposal of this biomass due to the environmental consequences of storage, landfill, or composting [24]. Thus, producing activated carbon from *Sargassum* may be economically viable and important in the sustainable development. Consequently, *Sargassum* species have been explored as biosorbent materials and precursors for the preparation of AC for water treatment [25–27]. The current research constitutes a commendable effort towards producing value-added commodities with low-cost biomass materials, specifically tailored for environmental applications.

Modification of carbon-based materials with innovative nanoscale materials provides several benefits, such as a porous structure, a high surface area, fast adsorption kinetics, and large adsorption capacities. Additionally, they offer a straightforward, inexpensive, and efficient means of eliminating contaminants from wastewater [28–30]. Covellite copper sulfide (CuS) NPs are extremely appealing due to their natural abundance of constituent elements, nontoxicity, low cost, and potential uses in a wide range of applications. CuS NPs are a potential material with two reactive soft atoms, and when applied in combination with carbon's reactive center and functional group, they have a greater variety of applications and a greater capacity to eliminate both inorganic as well as organic contaminants [31–33].

CuS NPs have been synthesized via wet chemical synthesis [34], microwave heating [35], sonochemical [36], hydrothermal [37], and green synthesis [38–41]. Despite the abundance of chemical and physical synthesis of CuS NPs in the literature, there are few green manufacturing methods that use microorgansims such as bacteria *Shewanella oneidensis* [39], the fungus *Fusarium oxysporum* [42], and the green alga, *Chlorella ellipsoidea* [33]. As a result, there is a growing trend towards employing green, economical, and nontoxic ways to synthesis CuS NPs. Very recently; we demonstrated the use of an aqueous algal *Sargassum siliquastrum* (*SS*) extract for the biosynthesis of monodisperised MnS nanospheres [43]. This species was found to have a wide range of beneficial bioactive chemicals, including terpenoids, sterols, sulfated polysaccharides, and polyphenols which act as reducing and capping agents to create NPs [44]. Hence, the goal is to assess if its aqueous extract may be utilized to actively govern the formation of a particular type of CuS NPs. Such biological entity–based NPs synthesis is projected to provide biocompatible, less toxic, and economically beneficial NPs [33].

The present study aims to valorize the invasive *Sargassum siliquastrum* alga by utilizing its biomass for the facile green synthesis of a simple, nontoxic, stable, and affordable nanoadsorbent (CuS NPs–AC) for the first time. The prepared sustainable nanoadsorbent was used for the adsorptive removal of EY as a model organic pollutant after the systematic characterization using FTIR, SEM, XRD, and BET. The batch technique was used to optimize a number of operational parameters, including pH, adsorbent dose, initial dye concentration, contact time, and temperature, for the highest EY removal. To fully understand the adsorption mechanism of EY dye onto CuS NPs–AC, various isotherm, kinetic, and thermodynamic studies were assessed and applied. Moreover, the investigation encompassed an analysis of the adsorption mechanism.

2 Experimental

2.1 Collection and preparation of algal material

Collection and preparation of *SS* alga were carried out from the Red Sea beach in Hurghada, Egypt, in May 2023 at 50–100 m from the beach in front of the National Institute of Oceanography and Fisheries (NIOF), 5 km north to Hurghada city at coordinates 27° 17′ 03″ N and 33° 46′ 21″ E) (Fig. 1). Briefly, alga were thoroughly washed with tap water, rinsed with deionized water, shade-dried for 15 days, oven dried at 60 °C, finely powdered, and stored at 4 °C. Ten grams of the powdered alga were extracted in 100 mL of deionized water (10%) and then used as a capping agent to create CuS NPs [43].
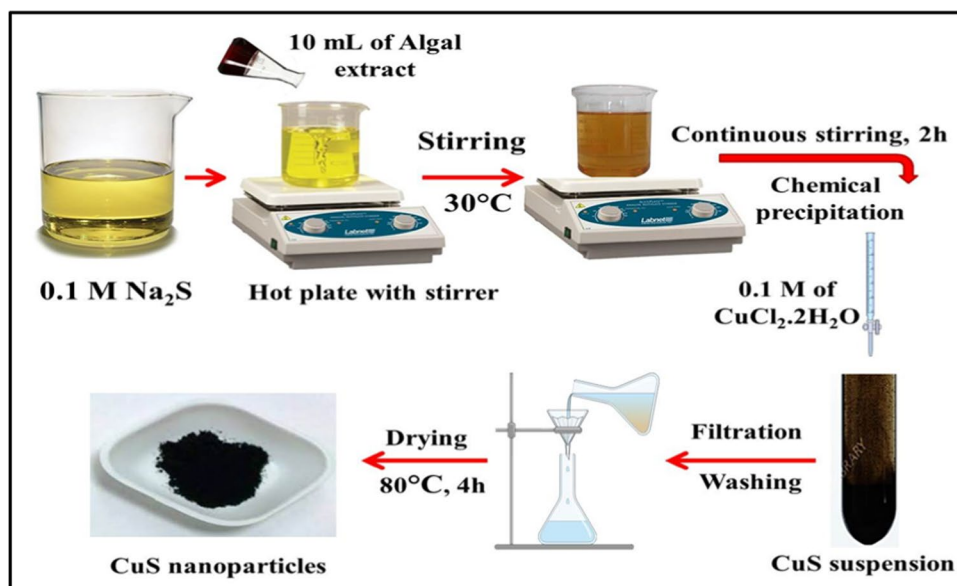
2.2 Preparation of AC

One hundred grams of the dried brown alga were gradually added to 100 mL of 98% H_2SO_4. At room temperature, the

Fig. 1 Photos of *SS* alga (**a** and **b**) and location map of sampling sites (**c**)
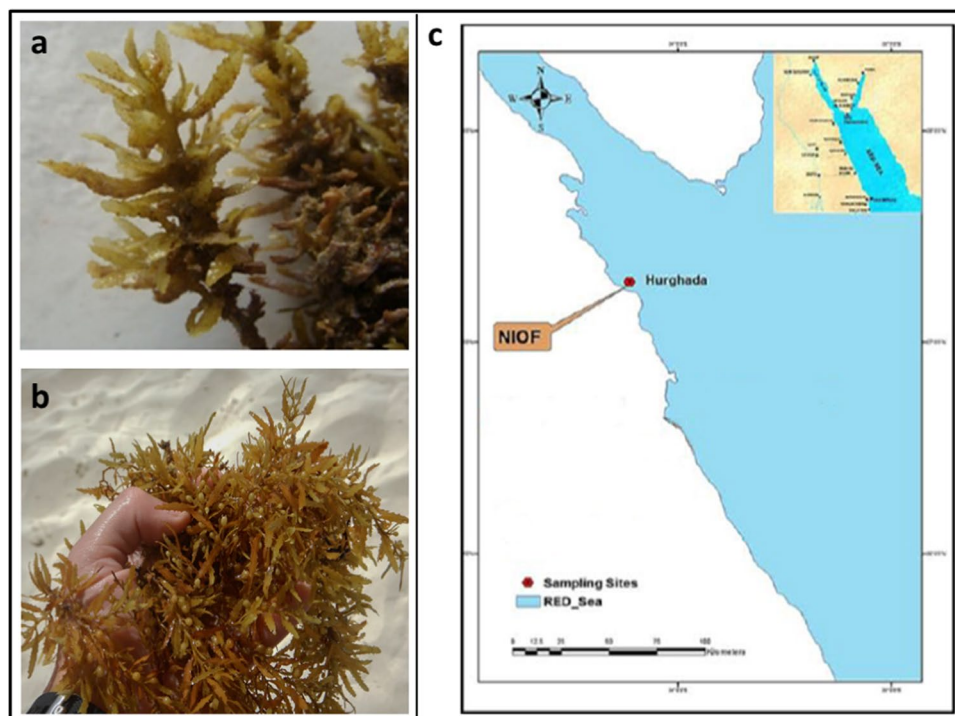
Scheme 1 Representation for the biosynthesis of CuS NPs

resulting mixture was kept for 24 h followed by refluxing for 2 h. After cooling to room temperature (25±2°C), the mixture was thoroughly rinsed with deionized water before being immersed in a 2% NaHCO$_3$ solution to neutralize any remaining acid. The resulting AC was dried at 100°C in an oven for 24 h and then stored until needed [45].

2.3 Biosynthesis of CuS NPs

At room temperature, 50 mL of sodium sulfide solution (0.1 M) were combined with 10 mL *SS* extract, and the mixture was vigorously stirred for 2 h. Fifty milliliters of a 0.1 M solution of CuCl$_2$.2H$_2$O were then drop-wise applied to the previous reaction mixture. To make sure the reaction was completed, a magnetic stirrer was used to agitate the solution for an additional hour. After completing the procedure, the precipitate was filtered, repeatedly washed with deionized water and ethanol to remove any remaining organic matter, and then dried for 4 h at 80°C [43]. Scheme 1 provides a schematic representation of the procedure for producing CuS NPs.

2.4 Preparation of CuS NPs–AC nanocomposite

CuS NPs–AC nanocomposite was produced in accordance with the literature with a few modifications [30]. About 1 g of CuS NPs was added separately into 20 mL of deionized water and the solution was homogenized on a magnetic stirrer for 30 min. After that, the resulting CuS NPs suspension was mixed with 1.0 g of AC in a 100-mL conical flask and then ultrasonicated for 30 min. The produced suspension was then subjected to a magnetic stirring for 2 h at 80°C to deposit CuS NPs on AC surface. The obtained suspension was decanted, filtered, and repeatedly washed with deionized

water. Finally, CuS NPs–AC nanocomposite was dried in an electric oven at 90°C for 12 h. Scheme 2 provides a schematic representation of the procedure for producing CuS NPs–AC nanocomposite.

2.5 Instrumentation for the characterization of CuS NPs–AC nanocomposite

The possible impact of phytochemicals of *SS* in the formation of CuS NPs and the surface functional groups of CuS NPs–AC nanocomposite were examined using FTIR spectroscopy in the 400–4000 cm^{-1} range (Shimadzu FTIR, Kyoto, Japan). The phase composition and crystal structure of the synthesized samples were examined by recording X-ray diffraction spectra using a powder diffractometer (Brucker D8 Advance, Germany in the range of 10° to 70°). Scherrer's equation was employed to calculate the average crystallite size. The morphology, size, and chemical composition of the produced nanocomposite were investigated using a SEM (Jeol JSM-IT200, Japan) that was attached with EDX from the same company. The specific surface area (SSA) was determined using NOVA touch 4LX analyzer from Quantachrome Instruments, USA. N$_2$ adsorption/desorption data were used to calculate the SSA value using the multipoint Brunauer-Emmet-Teller (BET) method. According to the Barrett-Joyner-Halenda (BJH) hypothesis, the average pore diameter was measured.

2.6 Study of point of zero charge (PZC)

The pH drift method [46] was modified slightly in order to determine the PZC of CuS NPs–AC. An aqueous solution of NaCl (0.01 M) and fixed sorbent loading (2.0 g/L) were

Scheme 2 Synthesis of CuS NPs–AC nanocomposite
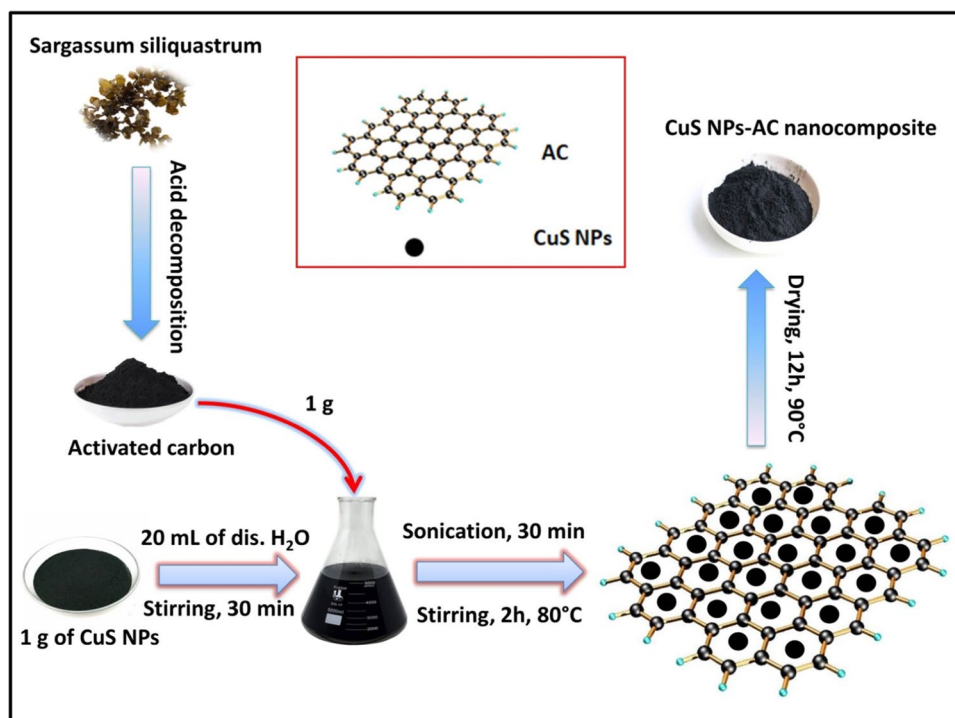
added to 50 mL reagent bottles, and the pH of each bottle was then adjusted with a solution of 0.1 M NaOH or 0.1 M HCl at a pH range (2–12). After that, the mixture was stirred for 48 h to bring it to equilibrium. The final reading for each solution was then calculated by measuring pH_f and pH_i was plotted against calculated ΔpH ($\Delta pH = pH_i - pH_f$). The PZC is the location where $\Delta pH = 0$. The pH meter was calibrated at pH 4, 7, and 10 prior to each run.

2.7 Adsorption experiments

A batch approach was used to conduct the adsorption studies as depicted in Scheme 3. Initial pH, adsorbent dosage, contact time, solution temperature, and initial EY concentration

of the solution were the parameters that were examined. 0.1 g of adsorbent and 100 mL of 100 mg/L EY were mixed and agitated in a temperature-controlled shaker at 298 K for 15 min as part of the batch pH study procedure. An UV-vis spectrophotometer (PG Instruments, model T80, UK) was used to quantify all concentrations at 517 nm. By adding diluted NaOH or HCl solutions, the initial solution pH values were adjusted to various values (2, 3, 5, 7, and 9). The pH meter was used to measure pH values (Mettler Toledo S220, Columbus, OH). Additionally, batch experiments were conducted at 298 K and the ideal pH value for 30 min of shaking time to investigate the effect of adsorbent dose. To this end, different amounts of CuS NPs–AC (0.02–0.12 g) were added into each 100 mL EY solution (100 mg/L). The

Scheme 3 EY batch adsorption process
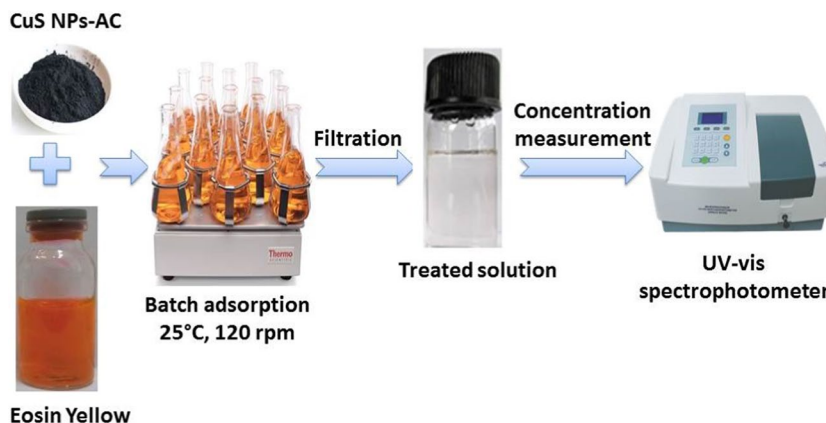
removal percentage of EY was calculated according to the following equation:

$$R\% = \left((C_o - C_e)/C_o \right) * 100 \tag{1}$$

where C_o and C_e (mg/L) are the initial and equilibrium concentrations of EY, respectively.

2.8 Equilibrium studies

A 100 mL EY solution with various initial concentrations (100–300 mg/ L, 50 mg/L interval) was shaked with 0.1 g of CuS NPs–AC at pH value of 7 at various temperatures (298, 308, 318, and 328 K) to study the adsorption isotherm and investigate the effect of initial concentration on EY elimination. The equilibrium was attained after 60 min of shaking at 120 rpm. An UV-vis spectrophotometer was used to assess EY concentrations after the suspensions had been filtered. EY uptake at equilibrium, q_e (mg/g), was calculated by the following equation:

$$q_e = \left(C_o - C_e \right) * (V/m) \tag{2}$$

Where V (L) is the volume of the aqueous EY solution, and m (g) is the weight of CuS NPs–AC used. The isotherm models provided by Langmuir, Freundlich, Temkin, and Dubinin-Radushkevich were assessed after the equilibrium concentration of EY was determined under different temperatures. Calculations were made to determine the various parameters relating to each model. The Langmuir model was utilized to determine the maximum adsorption capacity by CuS NPs–AC using the equilibrium data, verifying the monolayer's complete closure on the adsorbent surface. The Langmuir linear equation is denoted as follows [47],

$$C_e/q_e = \left(1/q_m \right) * Ce + 1/\left(K_L * q_m \right) \tag{3}$$

The apparent energy of adsorption is described by the symbol K_L, which stands for the adsorption equilibrium constant (L/mg). Absolute monolayer closure is indicated by the constant q_m (mg/g). A graph of C_e/q_e vs C_e produces a slope and intercept of a straight line, $1/q_m$ and $1/(K_L*q_m)$, respectively. Additionally, whether the adsorption process is favorable ('1), unfavorable (>1), irreversible (0), or linear (1) is determined by the Langmuir dimensionless constant R_L. The equation listed below can be used to determine the value of R_L [47].

$$R_L = 1/\left(1 + K_L * C_o \right) \tag{4}$$

On a non-ideal basis, the Freundlich isotherm model is utilized for adsorption incorporating heterogeneous sorption mechanisms. This model is generally described as follows [47].

$$\log\, q_e = (1/n)\, \log\, C_e + \log\, K_F \tag{5}$$

The distribution coefficient, K_F (mg/g), which describes the quantity of adsorbate adsorbed for a given equilibrium concentration, can be thought of as the amount of adsorbate per unit weight. The bonding energy in the adsorbent-adsorbate system can be represented by the constant n. A straight line of slope, $1/n$, and intercept, $\log K_F$, are produced by a graph of $\log q_e$ vs $\log C_e$. As opposed to the logarithmic assumption of the Freundlich isotherm model, the Temkin isotherm model predicts that the heat of adsorption will decrease linearly. The model is described as [48].

$$q_e = \beta * \ln\, C_e + \beta * \ln A \tag{6}$$

With $\beta = RT/b$, R denotes the universal gas constant (8.314 J/mol.K) and T the absolute temperature in Kelvin (K). The constant b stands for the heat of the adsorption process (J/mol). The Temkin isotherm constant A is expressed as L/mg. A slope of β and intercept of $\ln A$ can be seen in a graph of $\ln C_e$ versus q_e. The D-R model is a method for determining the adsorption properties and apparent free energy. Typically, this model is characterized in the following manner [4],

$$\ln\, q_e = -K\varepsilon^2 + \ln\, q_m \tag{7}$$

The adsorption system constant K_{ad} represents the adsorption energy, the Langmuir system constant q_m is given in mg/g, and the Polanyi potential is represented by ε which can be calculated by the following equation:

$$\varepsilon = RT * \ln\, \left(1 + 1/C_e \right) \tag{8}$$

K_{ad} is obtained from the slope of the straight line produced when $\ln q_e$ is plotted against ε^2, and q_m is estimated from the intercept. Additionally, the mean adsorption free energy, which is represented by E, is calculated as [4].

$$E = \left(1/\sqrt{2Kad} \right) \tag{9}$$

E is the change in free energy when a unit mole of ions is transferred from infinity in the liquid (reaction mixture) to the solid (adsorbent) surface.

2.9 Kinetic studies

Shacking 0.1 g of CuS NPs–AC with 100 mL of EY solution (200, 250, and 300 mg/L) at 298 and optimal pH value for 120 min was used to conduct adsorption kinetic experiments. The contact times were set between 10 and 120 min. At various time periods, the amount of EY in the supernatant was measured. The results of the pseudo-first-order, pseudo-second-order, and Elovich models were applied to the data to determine the adsorption kinetics. The pseudo-first-order and the pseudo-second-order adsorption models' equations are given as follow [49]:

$$\ln\ (q_e - q_t) = \ln\ q_e - K_1 * t \tag{10}$$

$$t/q_t = (1/K_2 * q_e^2) + (1/q_e) * t \tag{11}$$

where q_e and q_t are the amounts of EY adsorbed on CuS NPs–AC (mg/g) at equilibrium time and at time t (min), respectively. K_1 is the rate constant of pseudo-first-order adsorption (min^{-1}), K_2 is the rate constant of second-order adsorption (g (mg. min) $^{-1}$).

The Elovich model assumes that there are no interactions between the species that are adsorbed, and that the energetically heterogeneous solid adsorbent surfaces actually exist. Based on a second-order reaction mechanism, these energetically heterogeneous adsorbent surfaces exhibit several types of activation energies [5]. The following equation is the linearization form of the Elovich kinetic model:

$$q_t = (1/\beta)\ \ln\ (\alpha\beta) + (1/\beta)\ \ln\ t \tag{12}$$

where α represents the initial adsorption rate ((mg/g).min^{-1}) and β represents the desorption coefficient related to the extent of surface coverage and activation energy for chemisorption ((g/mg).min^{-1}) respectively.

2.10 Data and error functional analysis

The data were analyzed using OriginPro 9.0 software. All experiments were done in triplicate to ensure reproducibility and data are expressed as mean ± standard deviation. Error function is the best optimization technique for assessing how well the equation fits the experimental data. Apart from the regression coefficient (R^2), three error functions such as sum of square error (SSE), reduced chi-square test (χ^2), and residual root mean square error ($RMSE$) were calculated to evaluate the best fit of the modeled equation to the experimental data [50].

2.11 Thermodynamic studies

In order to conduct adsorption thermodynamic tests, 0.1 g of CuS NPs–AC was shacked with 100 mL of EY solution containing (100, 150, 200, 250, and 300 mg/L) at various temperatures (298, 308, 318, and 328 K) and the ideal pH for 60 min. To assess the thermodynamic viability and create a picture of the adsorption process, three thermodynamic parameters: change in Gibbs free energy (ΔG°), enthalpy (ΔH°), and entropy (ΔS°), were determined. The calculation formulae are as follows [51]:

$$K = q_e/C_e \tag{13}$$

$$\Delta G° = -RT * \ln\ K \tag{14}$$

$$\ln\ K = \Delta S°/R - \Delta H°/RT \tag{15}$$

where K represents the adsorption equilibrium constant, R [8.314 J/ (mol·K)] represents the ideal gas constant, and T (K) represents the absolute temperature.

2.12 Effect of interfering ions and selectivity of CuS NPs–AC nanocomposite

CuS NPs–AC nanocomposite was used to study the impact of interfering cations (Na$^+$, K$^+$, Ca^{2+}, and Mg^{2+}) and anions (Cl$^-$, NO$_3^-$, SO$_4^{2-}$, and PO$_4^{3-}$) on the adsorption of EY at 100 mg/L. Under ideal experimental conditions, the adsorption of EY was carried out utilizing CuS-AC nanocomposite, and the amount of EY adsorbed was calculated. Like how EY's adsorption in a binary mixture of other dyes (methylene blue, malachite green, and crystal violet) was used to determine the selectivity of CuS NPs–AC nanocomposite. The same initial EY concentration of 100 mg/L, adsorbent dosage of 2 g/L, temperature of 298 K, contact period of 60 min, and pH of 7 were used for the tests. Equations (16) and (17) were used to get the distribution ratio (D) and selectivity coefficient (α).

$$D = ((C_o - C_e)/C_e) * 100 \tag{16}$$

$$\alpha = (D_{EY}/D_{Dye}) \tag{17}$$

2.13 Reusability study

The ability of an adsorbent to regenerate and be reused is essential in practical and large-scale applications. In order to evaluate the durability of CuS NPs–AC, regeneration and reuse studies were conducted for five successive runs. In the first run, 50 mL of EY solution (300 mg/L) was mixed with 2 g/L of CuS NPs–AC at pH 7 for 120 min. After that, the adsorbent was separated by centrifugation at 6000 rpm for 15 min and the supernatant was used to determine the amount of remaining EY by a UV-vis spectrophotometer as previously described. Finally, the collected CuS NPs–AC was washed three times with deionized water and ethanol mixture (1:1), dried in an electric oven for 2 h at 80°C, and then introduced to the next run.

3 Results and discussion

3.1 Biosynthesis of CuS NPs

CuS NPs were readily synthesized at ambient temperature (30°C) employing the proposed method, which involved the reaction of an aqueous solution of Cu^{2+} ions with S^{2-} ions in the presence of an aqueous *SS* extract (Scheme 1). According

to the pervious researches, *SS* possesses a variety of valuable bioactive molecules, such as terpenoids, sterols, sulfated polysaccharides, and polyphenols, which serve as capping agents to produce CuS NPs [44]. These biomolecules from *SS* extract are hypothesized to bind copper ions in the presence of sulfide ions, assisting in the synthesis of stable CuS NPs. Similar mechanism was proposed by Borah et al. [33] when used an aqueous extract of the green alga *Chlorella ellipsoidea* for the manufacture of Covellite CuS NPs. Equation 18 summarizes the overall synthesis process.

$$CuCl_2 + Na_2S \xrightarrow{\text{Biomolecules of } SS \text{ aqueous extract}} CuS + 2NaCl$$

(18)
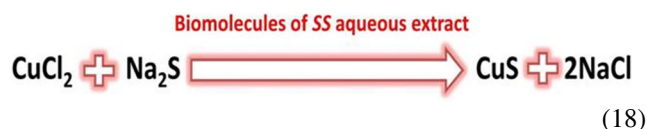
3.2 Adsorbent characterization

3.2.1 FTIR

FTIR was used to assess surface characteristics and examine the functional groups present on the adsorbent's surface, which enables for adsorption performance. Surface functional groups responsible for EY absorption were studied in this study. The FTIR spectrum showed that AC had a large number of peaks (Fig. 2a). This indicates the complex nature of AC. FTIR spectrum of AC shows three distinct bands at 3550.31, 3483.78, and 3412.42 cm^{-1} which assigned to NH or OH stretching vibrations in agreement with Yamil et al. [52] who prepared activated carbon from queen palm endocarp with a high adsorptive performance for the herbicide 2,4-dichlorophenoxyacetic acid (2,4-D).

The asymmetrical and symmetrical stretching vibrations of CH$_3$ and CH$_2$ groups of aliphatic compounds may be related to the bands found at 3235.97 and 2925.48 cm^{-1}, similarly in a study of activated carbon from the mandacaru cactus (*Cereus jamacaru*) for removal of Basic Fuchsin from aqueous solutions which reported by Georgin et al. [53]. The weak band at 2130 cm^{-1} was due to the stretching vibration of C-C=O. The stretching vibration of C=O and C=C can be assigned to the bands at 1638.23 and 1617.02 cm^{-1}, respectively. This agree with a study reported by Georgin et al. [54] when employed a high porous activated carbon from *Jacaranda mimosifolia* for remarkable removal of aqueous-phase ketoprofen. The peaks at 1523 and 1438 cm^{-1} may be related to the aromatic rings model [53]. OH bending vibration is assigned to the FTIR band at 1370 cm^{-1} [55]. The C-O stretching of secondary and primary alcohols is ascribed to the FTIR bands at 1154 and 1057 cm^{-1} [56, 57]. NH$_2$ bending is responsible for the vibrational bands from 800 to 600 cm^{-1} [58]. The existence of vibrational peaks at 671 and 618 cm^{-1} in the FTIR spectrum of CuS NPs suggests the presence of Cu–S stretching modes, whereas the peak at 1120 cm^{-1} corresponds to C–O stretching of the adsorbed CO$_2$ molecules (Fig. 2a) [59]. The FTIR spectra of CuS NPs–AC exhibited the characteristic peaks of both CuS NPs and AC after introducing CuS onto the surface of AC. It is evident that the location and intensity of the peaks in the nanocomposite have changed (Fig. 2a), which likely explains the successful loading of CuS on the surface of activated carbon. Similar trend was reported by Yang et al. 2022 [60] as they loaded copper sulfide particles on carbon black obtained from used tires to develop an efficient adsorbent for removing of mercury (II) from aqueous solution.

Fig. 2 FTIR (**a**) and XRD (**b**) of the prepared AC, CuS NPs, and CuS NPs–AC
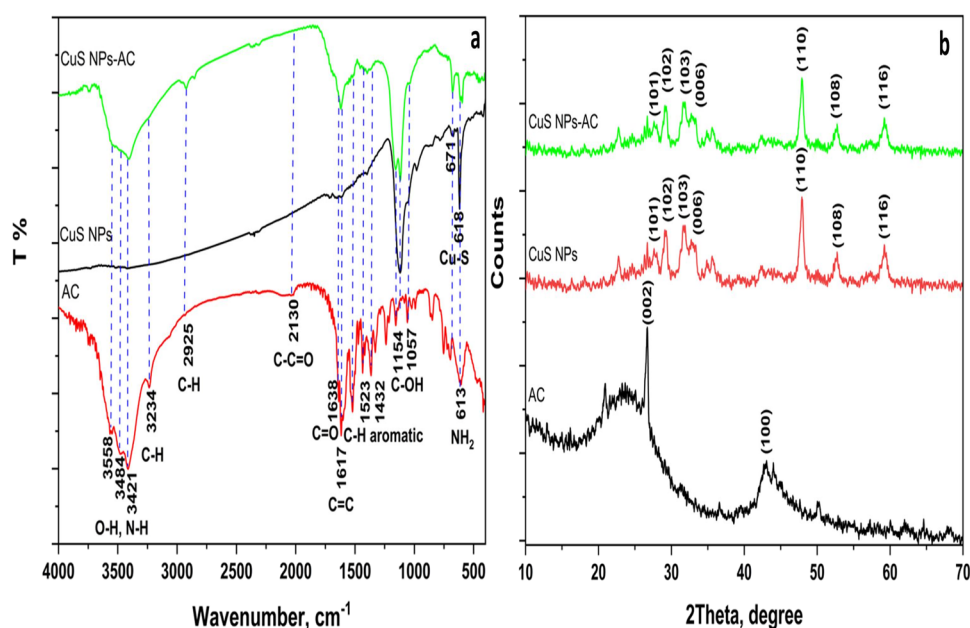
3.2.2 XRD

Powder X-ray diffraction is used to examine the crystalline structure and lattice parameter of the prepared adsorbent. Figure 2b shows the XRD pattern of the activated carbon. The turbostratic structure of the activated carbon is in accordance with previous results on graphitic carbon diffraction planes including randomly oriented micro crystallites [61]. The superposition of several aromatic layers in the activated carbon results in the creation of micro crystallites. Two broad peaks are shown at 2θ values of 26° and 43°, respectively, which correspond to the (002) and (100) planes. The absence of any distinct peaks in the XRD spectrum suggests that the activated carbon has a porous, amorphous structure, which is a substantial factor for its adsorption capacity and making it the perfect substrate for the synthesis of nanocomposite materials [61]. Amorphous materials typically have large porosity, which facilitate the accommodation of adsorbate molecules on the adsorbent surface and make them as realistic as adsorbents [62]. The CuS nanoparticles' X-ray diffraction pattern is shown in Fig. 2b. The diffraction pattern and interplanar spacing observed were quite like the CuS standard diffraction pattern. The (101), (102), (103), (006), (110), (108), and (116) reflection lines of Covellite CuS were assigned to the peaks at 2θ = 27.68°, 29.27°, 31.78°, 32.88°, 47.93°, 52.72°, and 59.36°. They were consistent with CuS's normal hexagonal Covellite phase ((JCPDS card no. 06-0464)) [63]. The XRD pattern revealed no typical peaks of any contaminants such as CuO or Cu(OH)$_2$, indicating that high-quality CuS was generated by our method. The average crystallite size of the produced CuS NPs is determined to be 12.7 nm using the Debye Scherer equation. Similar results were obtained by Borah et al. [33] when devised a green method for the synthesis of Covellite CuS NPs using aqueous extract of a green alga, *Chlorella ellipsoidea*. The diffraction peaks of CuS NPs–AC nanocomposite are consistent with as-prepared CuS NPs (Fig. 2b), and the characteristic peaks of AC are less apparent, which is probably due to the covering of the weak and broad peaks of AC by the strong diffraction peaks of CuS NPs [63].

3.2.3 SEM

Scanning electron microscopy is a useful tool for identifying the morphological features of the prepared samples. Figure 3a–c shows SEM images of as-prepared AC, CuS NPs, and CuS NPs–AC, respectively. The results of the SEM investigation of AC at X8000 magnification are shown in Fig. 3a. The SEM image showed a porous surface that was uneven and had cavities, giving it a heterogeneous character. The more heterogeneity of activated carbons surface, the more likely it is that the material will have superior

adsorptive performance because of the abundance of features and the resulting rise in specific surface area [64]. Additionally, the multiporous surface with cavities plays a significant role in adsorption capacity. This result was in agreement with the previous reports for activated carbons derived from packaging waste [19], coconut shell [46], Queen palm fruit endocarp (*Syagrus romanzoffiana*) [52], *Jacaranda mimosifolia* seed pods [54], and Brazil nutshells [55] which were used for the adsorption of carbon dioxide, methylene blue, 2,4-dichlorophenoxyacetic acid herbicide, ketoprofen, and acetaminophen, respectively. The surface morphology suggested that the mechanism of eosin dye adsorption may have incorporated diffusion process [65]. Figure 3b displays the distinctive SEM picture of pure CuS NPs. Granular aggregates can be observed in this image having irregularly shaped, rough-surfaced particles of varying sizes. In the presence of porous AC, the morphology of CuS NPs changes from irregular shape to coral reef structure in as-prepared CuS NPs–AC nanocomposite (Fig. 3c). Furthermore, CuS coral reefs formed on the surface of the fabricated porous AC on a regular basis. The findings indicate that the addition of porous AC materials with a large surface area can alter the morphology of CuS and, to some extent, prevent CuS agglomeration, resulting in an increase in the specific surface area of CuS NPs–AC nanocomposite. These findings agreed with those reported by Li et al. [63] where they employed one-step solvothermal method to prepare CuS nanosheets–based 3D micro-flowers grown on pomelo peel-derived porous activated carbon for high-performance supercapacitors.

3.2.4 EDX analysis

The elemental composition and purity of the produced samples were also determined by EDX analysis. According to the EDX spectra of the pure AC, C (60.32%), O (34.32%), Ca (4.76%), Si (0.1%), and Na (0.51%) by weight were present (Fig. 3d). Since carbon (C) is the most abundant element, the dried SS seaweed sample was likely thoroughly carbonized. It is possible to see the presence of inorganic elements like oxygen (O) and silicon (Si). The availability of oxygen (O) indicates that they are present on the carbon surface. Mineral compounds, such as Ca and Na, can also be found in small amounts in AC sample [66]. The EDX spectrum of the synthesized CuS NPs is shown in Fig. 3e. The product is exceptionally pure, as evidenced by the well-defined, sharp, and clear peaks of the spectrum, with the corresponding peaks for Cu and S having an average mass percentage ratio of 66.7:33.3. The presence of the corresponding elements in the stoichiometric ratio was also confirmed. Furthermore, no other element-related signals were detected in the generated sample, indicating that the nanoparticles were devoid of impurities. EDX peaks of CuS NPs
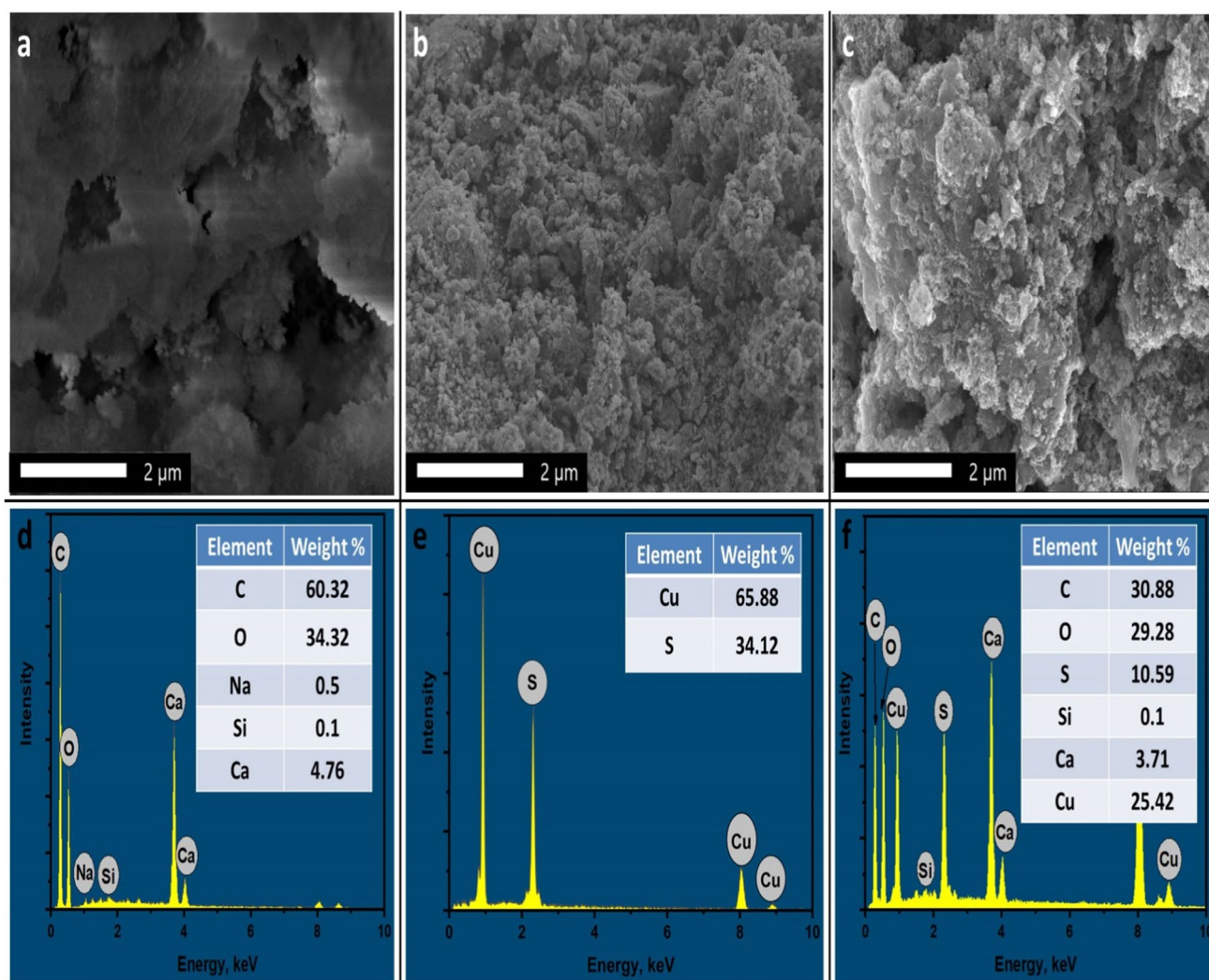
Fig. 3 SEM images of AC (**a**), CuS NPs (**b**), and CuS NPs–AC (**c**) at ×8000 magnification, and EDX profiles of AC (**d**), CuS NPs (**e**), and CuS NPs–AC (**f**)

are also matched with XRD peaks which are evidence of the purity of the sample. Due to the loading of CuS NPs on AC, nearly 25.42% of Cu and 10.59% of S were present in the CuS NPs–AC. The results show that the CuS NPs are uniformly distributed across the surface of the AC (Fig. 3f). Additionally, variations in the atomic and mass proportions of carbon and oxygen have also shown that CuS NPs were successfully loaded.

3.2.5 TEM and SEAD analyses of CuS NPs

TEM is used to study the topographical, morphological, and particle size information of the biosynthesized CuS NPs as shown in Fig. 4a and b. TEM images of CuS NPs show aggregates with the majority of spherical particles and a few nanoparticles with tetrahedron structure. The diameter of nanoparticles varies from 16 to 28 nm. The small particle

size of CuS NPs can be explained by the capping action of the biologically active chemical compounds in *SS* extract, which prevented the creation of large nanoparticles [33]. The lattice fringes are a sign of good crystallinity. In good agreement with the XRD diffraction profile, the selected area electron diffraction (SAED) patterns showed concentric rings indexed to several crystal planes of CuS hexagonal phase (Fig. 4c). Similar results were reported by [33]. As a result, the described synthetic approach was successful in producing highly pure CuS NPs with small particle size.

3.2.6 BET analysis

The surface area of the adsorbent is critical in the adsorption process. Adsorbent materials with a larger surface area and pore size are favored. Adsorbate molecules have a larger possibility of being adsorbed due to larger surface

Fig. 4 TEM images (**a** and **b**) and SAED (**c**) of the biosynthesized CuS NPs
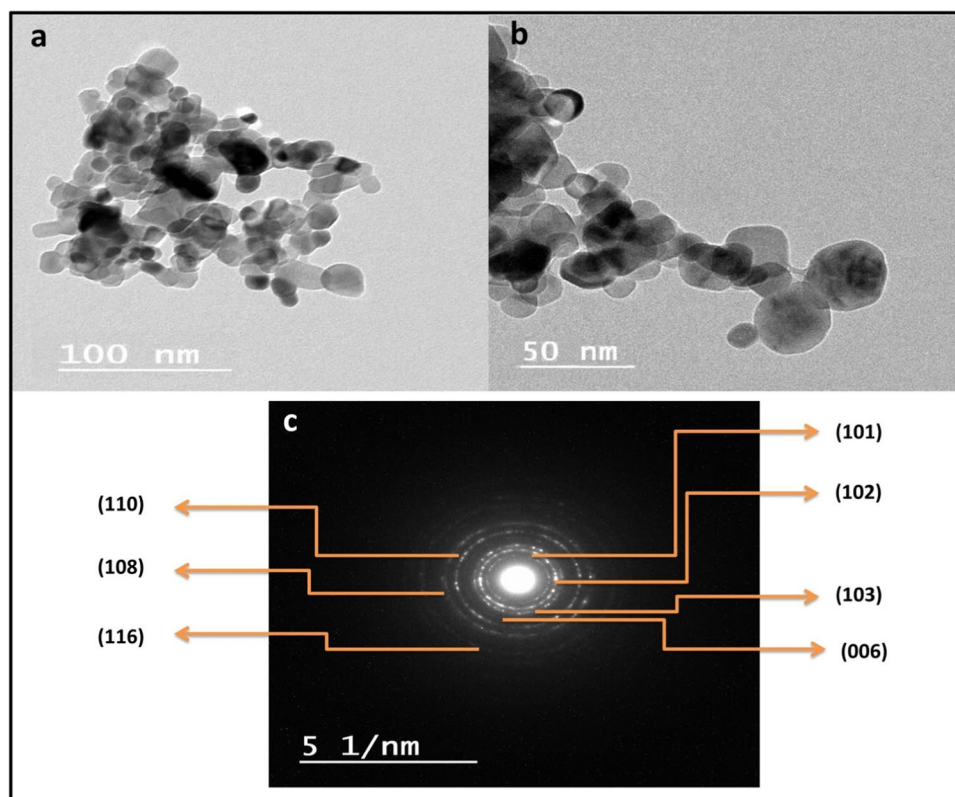
area. Furthermore, larger pore size accommodates more dye molecules [67]. It is well known that the physical properties of activated carbon-based adsorbent, such as porosity, pore volume, surface area, and pore size, can be used to determine the material's adsorption capability [68]. The N_2 adsorption-desorption isotherm plot of CuS NPs–AC is shown in Fig. 5a. According to the IUPAC classification, the isotherm (Fig. 5a) displays a type IV isotherm, suggesting the mesoporous structure of CuS NPs–AC. The latter is a feature of slit-shaped pores and was abundant in the material as detected by capillary condensation at relative pressure (P/P^{o}) values greater than 0.8. The textural properties as obtained from BET analysis are surface area of 367.184 m^2/g, and pore volume of 0.4595 cm^3/g (Fig. 5b). The BJH average adsorption pore diameter was 3.84 nm (2–50 nm), which also indicated that CuS NPs–AC exhibited a mesoporous structure according to the IUPAC classification (Fig. 5c). In addition, the estimated diameter of EY was 1.07 nm [4], indicating that EY could easily enter CuS NPs–AC pores. Thus, the surface area and mesopore volume of CuS NPs–AC were found to be enormous, indicating a great potential for adsorption of EY.

3.2.7 PZC

By using PZC or isoelectric point, the active centers that are present on the surface are evaluated. Figure 5d displays the isoelectric point for CuS NPs–AC determined by graphing ΔpH against pH$_i$. PZC is the pH at which all charges on a material's surface are zero [69]. This is a key ingredient in the adsorption process because it indicates the pH range in which cationic or anionic dye can be effectively adsorbed. Due to the adsorbent's positively charged surface, anionic dye adsorption is more realistic at pH‹ PZC. However, because of the negative group, such as the OH$^-$ group, on the surface at pH› PZC, the cationic dye adsorption is more feasible. The PZC of CuS NPs–AC is around 7, and at this point, its surface charge is neutral. Therefore, at pH values lower than PZC, CuS NPs–AC surfaces carry positive charges and respond more effectively with EY. The surface of CuS NPs–AC has a negative charge when the pH is higher than PZC, which makes them less effective for removing EY from wastewater. Thus, it has been demonstrated that the EY dye will attach to the surface of the adsorbent more effectively at acidic pH range (lower than 7).
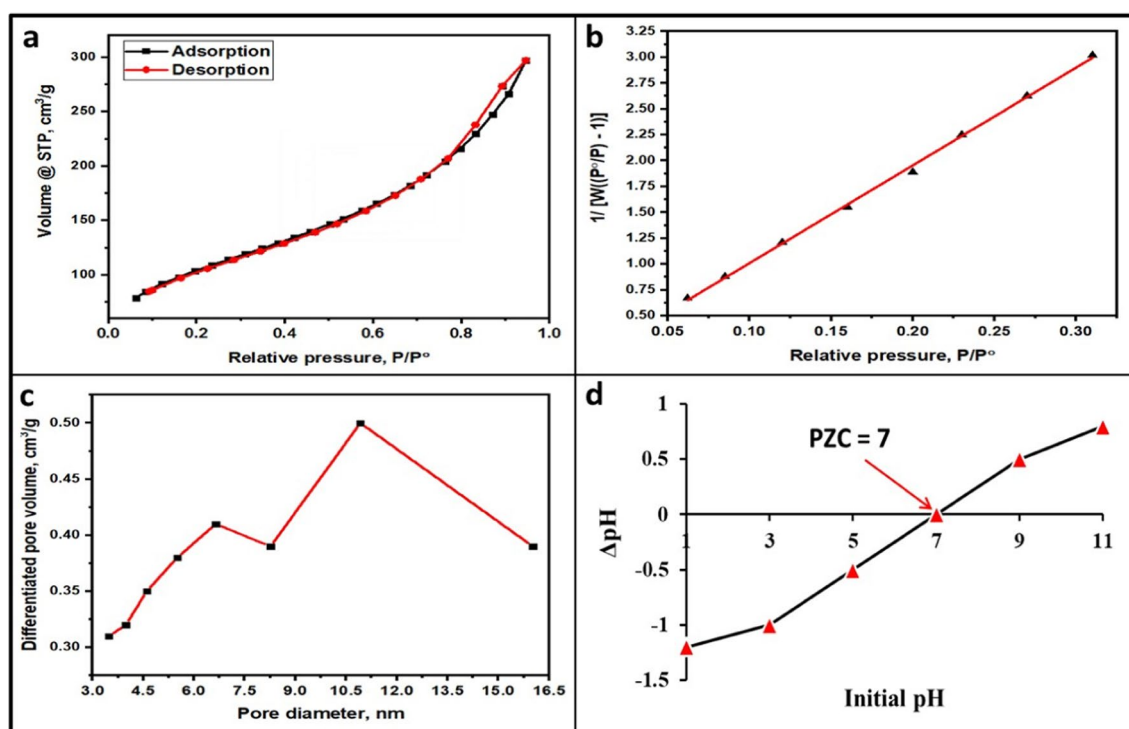
Fig. 5 N$_2$ adsorption/desorption isotherm (**a**), BET plot (**b**), BJH plot (**c**), and PZC of the prepared CuS NPs–AC (**d**)

3.3 Studying the effective parameters on EY adsorption by CuS NPs–AC

3.3.1 Effect of solution pH

Using a dye concentration of 100 mg/L and a 2 g/L adsorbent dose at 298 K, the effects of pH on EY removal by CuS NPs–AC were investigated over a wide pH range (pH 2–9). The addition of 0.1 M NaOH and 0.1 M HCl was utilized to control the solution pH. Figure 6a displays the dye adsorption capacity and percentage at various pH values. The dye molecules undergo structural changes due to protonation or deprotonation as a result of pH variation, and these changes are what cause the dye molecules to bind to the adsorbent sites through hydrogen bonds or electrostatic interactions [70]. Additionally, the pH-dependent variation of the surface functional groups of the adsorbent affects how dye is absorbed by CuS NPs–AC. At acidic pH levels (pH < 7), the CuS NPs–AC's OH and NH$_2$ groups have the potential to become protonated and form bonds with anionic dyes. Similar to this, at a basic pH (pH> 7), deprotonation of OH and NH$_2$ groups result in a negatively charged surface on the CuS NPs–AC, this makes cationic dye binding easier. The presence of varying amounts of different functional groups in CuS NPs–AC makes it is crucial to investigate the dominant surface charge at a specific pH. This was accomplished by determining PZC of the adsorbent. This

aids in understanding how the adsorbent interacts electrostatically with anionic and cationic dyes. The PZC of CuS NPs–AC is determined as 7 (Fig. 5d) [71]. The maximum adsorption capacity of EY was seen at lower pH levels. According to Fig. 6a, the best conditions for EY adsorption on AC–CuS NPs were at pH 2, where the adsorption removal and capacity were 98.935±1% and 98.928±1.1 mg/g, respectively. The protonated surface of CuS NPs–AC may have interacted with the anionic groups of EY at low pH values (pH ‹ PZC), meanwhile the competition with OH⁻ ions for the adsorption sites of CuS NPs–AC at higher pH values (pH > PZC), resulting in a dramatic decrease in the amount of available adsorption sites [72]. This observation agrees with the pervious results where Bukhari et al. [65] and Nazir et al. [67] reported an optimum pH value of 2, Rashtbari et al. [51] and Oyelude et al. [73] reported pH 3, and pH 4 was reported by Mahmood et al. [47] and Bahramifar et al. [72]. Since EY still adheres to surfaces at higher pHs (pH > PZC), the electrostatic interaction between dye molecules and the adsorbent is not the only reason for adsorption. Other non-covalent interactions may also be existed such as van der Waals, hydrophobic, and dipole-dipole interactions [74]. Through π-π stacking interactions, the aromatic dye rings in CuS NPs–AC interact with the aromatic rings of EY [75]. Additionally, O⁻ and COO⁻ groups of EY have a strong binding affinity towards the protonated amino groups of CuS NPs–AC [76].
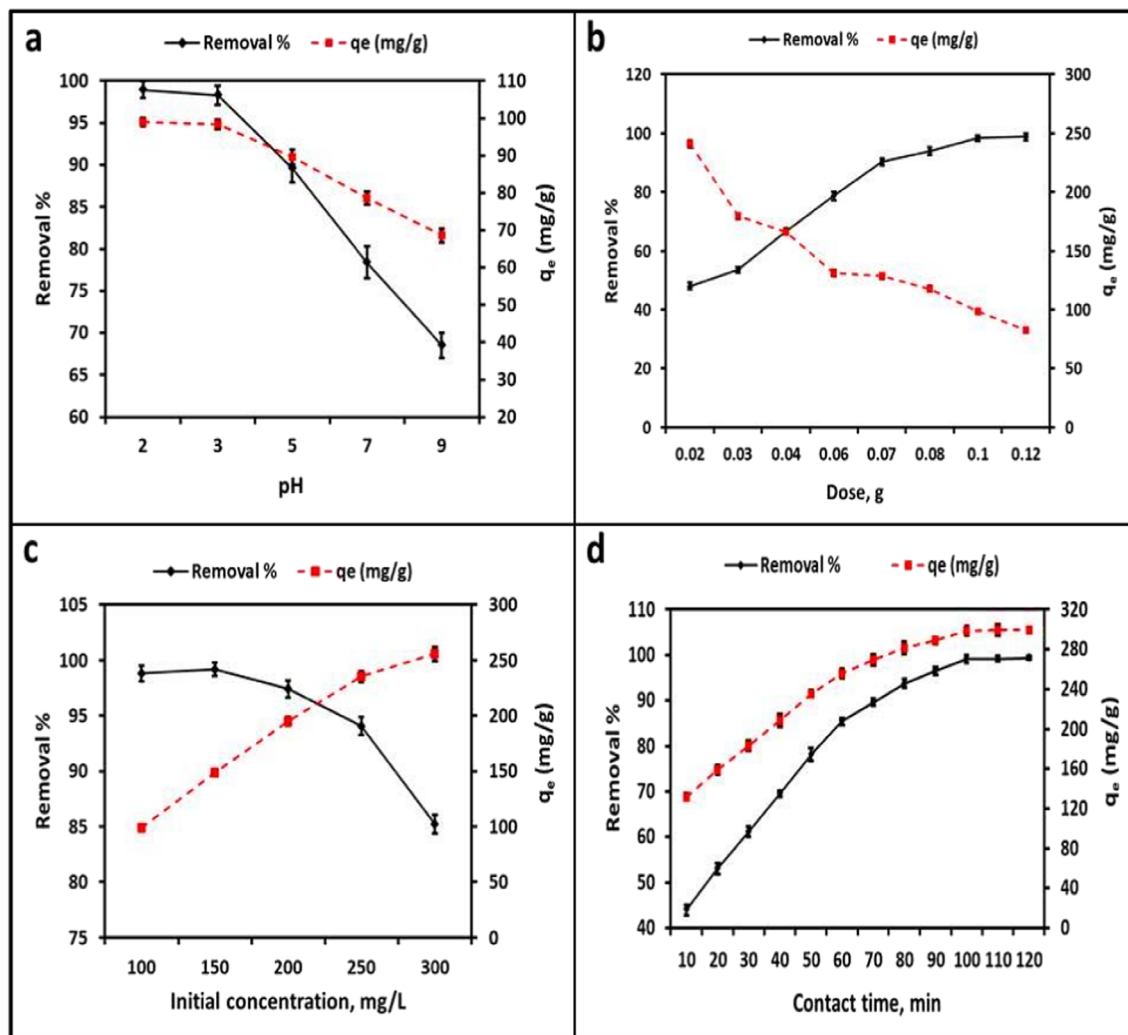
Fig. 6 Effects of operational parameters on EY adsorption removal and capacity; pH (**a**), CuS NPs–AC dose (**b**), initial EY concentration (**c**), and contact time (**d**)

In addition, eosin Y also contains C-Br bond, which creates the conditions for hydrogen bonding and halogen bonding with the amino and hydroxyl groups in CuS NPs–AC [77]. Additionally, the possibility of diffusion of these large dye molecules into the interiors between CuS NPs–AC exists due to the mesoporous nature of the adsorbent [78]. pH 7 was selected for EY adsorption onto CuS NPs–AC.

3.3.2 Effect of CuS NPs–AC dosage

Several researchers have documented the efficacy of various doses of adsorbents in adsorbing anionic dyes, with the aim of identifying the most economical and efficient dosage. The quantity of adsorbent used is a crucial factor as it greatly affects the adsorbent's capacity to adsorb EY at a given initial concentration. AC exhibits a superior removal capacity compared to other materials due to its porous structure

and distribution of pore sizes. This capacity is influenced by the adsorbate's polarity, solubility, and molecular size [79]. By adding an amount of CuS NPs–AC in the range of 10–120 mg to 100 mL of a 100 mg/L EY solution at pH 7, it was possible to investigate the impact of adsorbent dosage on EY adsorption; the results are shown in Fig. 6b. As the amount of adsorbent increased up to 120 mg, the percentage of EY removed by adding CuS NPs–AC increased from 48.06 ± 1 to $98.8\pm0.95\%$. The increase in EY removal with the rise in the adsorbent quantity may be attributed to the greater number of active sites available on the adsorbent's surface, which enhances the accessibility of adsorbate molecules. The adsorption capacity dropped from 241.3 ± 2.44 to 82.5 ± 1.2 mg/g as the adsorbent dosage was increased, in contrast to the removal percentage. This was due to the fact that as adsorbent concentration increased, the accessibility of high energy adsorbent active sites decreased and a greater

proportion of active sites with lower energy were occupied, resulting in a reduction in adsorption capacity [80]. There are some other adsorbents such as ferroferric oxide/polypyrrole magnetic composite [49], zinc oxide nanoparticles loaded on activated carbon [51], lemon peel–based low-cost biosorbent [65], tri-metallic-layered double hydroxide nanosheets [67], and teak leaf litter powder [73] recorded similar effect of adsorbent dose when utilized for EY uptake. Beyond 100 mg of the combined dose of CuS NPs–AC for EY, nevertheless, no remarkable changes in EY removal were observed. It can be explained by the agglomeration effects, which frequently cause adsorbent sites to collapse [4]. In light of this, it can be said that CuS NPs–AC is a highly effective adsorbent and that large amounts of both cationic and anionic dyes can be quickly adsorb using low doses of it. As a result, the amount of 100 mg of adsorbent/100 mL dye solution was chosen for further study.

3.3.3 Effect of initial EY concentration

An important variable in adsorption studies is the effect of initial concentration because it tells researchers the ideal amount of adsorbate to use to completely saturate the active sites on the adsorbents [81]. Figure 6c displays the plots of the adsorption capacity and percentage of CuS NPs–AC as a function of initial EY concentration. In Fig. 6c, the adsorption amount gradually increased from 98.797 ± 0.68 to 255.48 ± 0.84 mg/g while the removal efficiency decreased from 98.817 ± 0.77 to $85.22\pm0.67\%$ as the initial dye concentration increased from 100 to 300 mg/L. The cause may be attributed to the possibility that higher initial dye concentrations can act as a powerful driving force for the transfer of dye molecules from the liquid phase to the solid phase, improving the occupancy of adsorption sites on CuS NPs–AC that is enhancing adsorption capacity [82]. However, for CuS NPs–AC with fixed mass, the number of available adsorption sites is constant. As a result, removal efficiency decreases when dye concentrations are higher because some dye molecules cannot be effectively captured [82].

3.3.4 Effect of agitation time

At different time intervals (10–120 min, 10-min interval), with an initial EY concentration of 300 mg/L, an adsorbent dosage of 2 g/L, and a temperature of 25°C, the rate of adsorption of EY by CuS NPs–AC was investigated. The obtained results are shown in Fig. 6d. From 0 to 120 min of contact time, EY removal capacity and efficiency increase, and after 120 min, equilibrium is reached. Similar findings were made by other researchers, who discovered that EY adsorption rises as contact time increases [73–78]. However, the rate of adsorption reported in this work is much faster than what has been reported on the adsorption of eosin Y on

other materials. Sharma et al. [3] reported equilibrium time of 960 min, Lawal et al. [6] reported 600 min, Abdus-Salam et al. [81] reported 240 min, and a 300 min was reported by Yu et al. [82]. The removal efficiency increased from 43.93 ± 1.14 to $99.4\pm0.45\%$ by increasing the treatment time from 10 to 120 min, which may be due to the increased number of active surface sites on CuS NPs–AC that are available for EY adsorption as well as the increased concentration gradient of EY in solution and in the adsorbent [82]. This is shown in the plot in Fig. 6d, where approximately $43.93\pm1.14\%$ of EY was absorbed by CuS NPs–AC within 10 min in the beginning. At the same time, the adsorption capacity increased from 131.66 ± 1.6 to 299.22 ± 2 mg/g. Due to the saturation of accessible adsorption sites, the adsorption of EY is slowed down in the later stages [82]. The results show that AC–CuS NPs have superior adsorption performance and high adsorption kinetics.

3.3.5 Effect of operating temperature

Adsorption tests at various temperatures (298, 308, 318, and 328 K) and contact time of 60 min were conducted using EY in a range of concentrations (100–300 mg/L) with a 0.1 g dosage of adsorbent. The effect of temperature on the adsorption of EY onto CuS NPs–AC nanocomposite at various temperatures in the test solution is depicted in Fig. 7. Over the entire concentration range, the removal percentage and adsorption capacity increased with rising temperatures. This could be explained by the dye molecules gaining enough kinetic energy as the temperature increases to cling to CuS NPs–AC surface. Additionally, there is an increase in EY-adsorbent surface collisions, which is a sign of an endothermic adsorption process [83]. Furthermore, a high temperature favors a reduction in solution viscosity and an acceleration of dye molecule movement [82]. As a result,
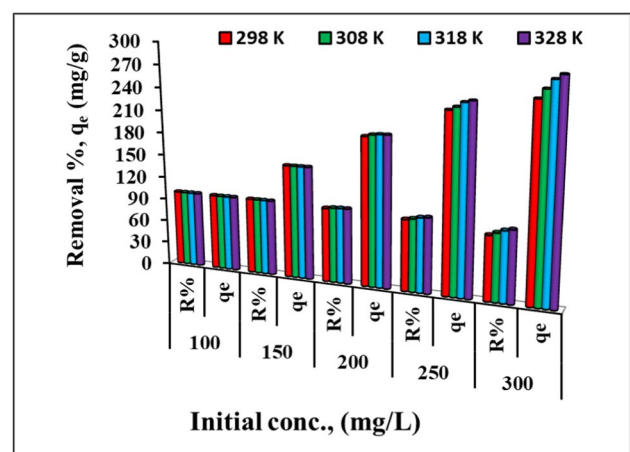

Fig. 7 Effect of operating temperature on EY adsorption removal and capacity

the CuS NPs–AC adsorbent and EY molecules can make more contact with one another, increasing the amount of dye that can be absorbed at high temperatures. The amount of adsorption did not, however, significantly increase as the temperature rose. Therefore, 298 K might be the ideal starting temperature for research. As a result, the adsorbent can be used to treat surface water at various temperatures without losing any of its adsorbent efficiency.

3.4 Analysis of adsorption equilibrium isotherms

To investigate the correlation between the equilibrium concentration of EY in solution and the quantity of EY adsorbed per unit weight of CuS NPs–AC, we utilized and confirmed four distinct adsorption isotherms. These isotherms were proposed by Freundlich, Langmuir, Temkin, and Dubinin and Radushkevich (D-R). The relevant parameters for each model were calculated.

3.4.1 Langmuir isotherm

The Langmuir isotherm model is appropriate for describing the adsorption of the EY dye on an adsorbent surface that has a specific number of adsorption sites occupied by a monolayer of the adsorbate. The model presupposes homogenous adsorption energy on the adsorbent surface and that solute molecule transmigration does not take place on the adsorbent's surface [47]. Table 1 lists the variables related to the Langmuir isotherm model for EY dye elimination. According to the Langmuir isotherm and the correlation coefficients, EY adsorption on CuS NPs–AC should be very positive. The high correlation coefficient, R^2, which was higher than 0.989, demonstrated the applicability of the Langmuir isotherm model to CuS NPs–AC. This supports the claim that the Langmuir isotherm model effectively represents the adsorption experiment. The R^2 values are, respectively, 0.999, 0.999, 0.997, and 0.989 at the four

Table 1 Adsorption isotherm constants of EY onto 0.1 g of CuS NPs–AC at 100–300 mg/L of initial EY concentration, pH = 7, 60 min contact time, and different temperatures (298–328 K)

Model	Parameter	Temperature (K)			
		298	308	318	328
Langmuir	q_m (mg/g)	263.16	277.78	294.12	303.03
	K_L (L/mg)	0.63	0.73	0.97	1.1
	R_L	0.005–0.016	0.0045–0.014	0.0034–0.01	0.003–0.009
	R^2	0.999	0.999	0.997	0.989
	SSE	6.41×10^{-6}	4.33×10^{-5}	1.25×10^{-4}	1.72×10^{-4}
	$RMSE$	0.0015	0.0038	0.0065	0.0078
	χ^2	2.14×10^{-6}	1.44×10^{-5}	4.17×10^{-5}	5.47×10^{-5}
Freundlich	$1/n$	0.223	0.233	0.251	0.244
	K_F (mg/g)	121.31	130.71	145.46	160.08
	R^2	0.840	0.762	0.652	0.470
	SSE	0.018	0.029	0.045	0.071
	$RMSE$	0.077	0.098	0.123	0.155
	χ^2	0.006	0.01	0.015	0.024
Temkin	B	38.758	42.295	47.809	48.497
	A (L/mg)	22.89	23.17	23.77	27.69
	R^2	0.922	0.868	0.774	0.593
	SSE	1272.10	2454.72	4753.22	9124.62
	$RMSE$	20.59	28.60	39.80	55.15
	χ^2	424.03	818.24	1584.41	3041.54
D-R	q_s (mg/g)	235.83	255.26	283.67	313.03
	K	3e−7	3e−7	2e−7	2e−7
	E (kJ/mol)	1.3	1.3	1.6	1.6
	R^2	0.929	0.908	0.851	0.663
	SSE	0.042	0.059	0.102	0.242
	$RMSE$	0.118	0.140	0.185	0.284
	χ^2	0.014	0.02	0.03	0.08

temperatures under investigation (298, 308, 318, and 328 K). The slope and intercept of the Langmuir formula were used to determine the q_m and K_L values (Eq. 3) (Fig. 8a). At 298 K, 308 K, 318 K, and 328 K, respectively, CuS NPs–AC showed theoretical maximum monolayer adsorption capacities of 263.16, 277.78, 294.12, and 303.03 mg/g which indicate the favorable adsorption with the increment of temperature. Furthermore, q_{max} values of the Langmuir isotherm were more closely aligned with the experimentally obtained values at the given temperature range (255.8, 267.8, 279.5, and 285.8 mg/g at 298, 308, 318, and 328 K, respectively) and higher than other adsorbents that have been reported in the literature such as xanthan-acacia hybrid super-adsorbent (4.17 mg/g) [3], zinc oxide nanoparticles loaded on activated carbon (163.9 mg/g) [51], lemon peel (8.240 mg/g) [65], clay/carbon composite (11.15 mg/g) [77], composite of goethite/thermally activated charcoal derived from date palm seeds (30.30 mg/g) [81], and polyethyleneimine-grafted polyphosphazene microspheres (92.34 mg/g) [82]. The K_L values, which are correlated with the adsorption energy, were between 0.63 and 1.1 L/mg at various temperatures. Additionally, all of the estimated R_L values fell between 0

and 1, demonstrating the favorable nature of EY adsorption onto CuS NPs–AC. Accordingly, we may reveal EY is sorbed onto CuS NPs–AC by a chemical mechanism.

3.4.2 Freundlich isotherm

The heterogeneous adsorption that results from the variety of adsorption sites on the absorbent is evaluated by the Freundlich model [48]. When a graph of log C_e against log q_e is displayed, a linear line with gradient, $1/n$, and intercept, log K_F (Fig. 8b). If the value of $1/n$ is less than unity, the adsorption is assumed to support the Langmuir isotherm model; if it is greater, cooperative adsorption is assumed. The process becomes increasingly heterogeneous as it gets closer to zero, implying the strength of adsorption heterogeneity [84]. Table 1 shows the Freundlich constants derived from the Freundlich plot. The correlation coefficient for this model was lower than that of the Langmuir model (0.84, 0.76, 0.65, and 0.47 at 298, 308, 318, and 328 K, respectively). Moreover, the size of the parameter $1/n$ also suggested that Langmuir model is better appropriate for the EY dye adsorption process.
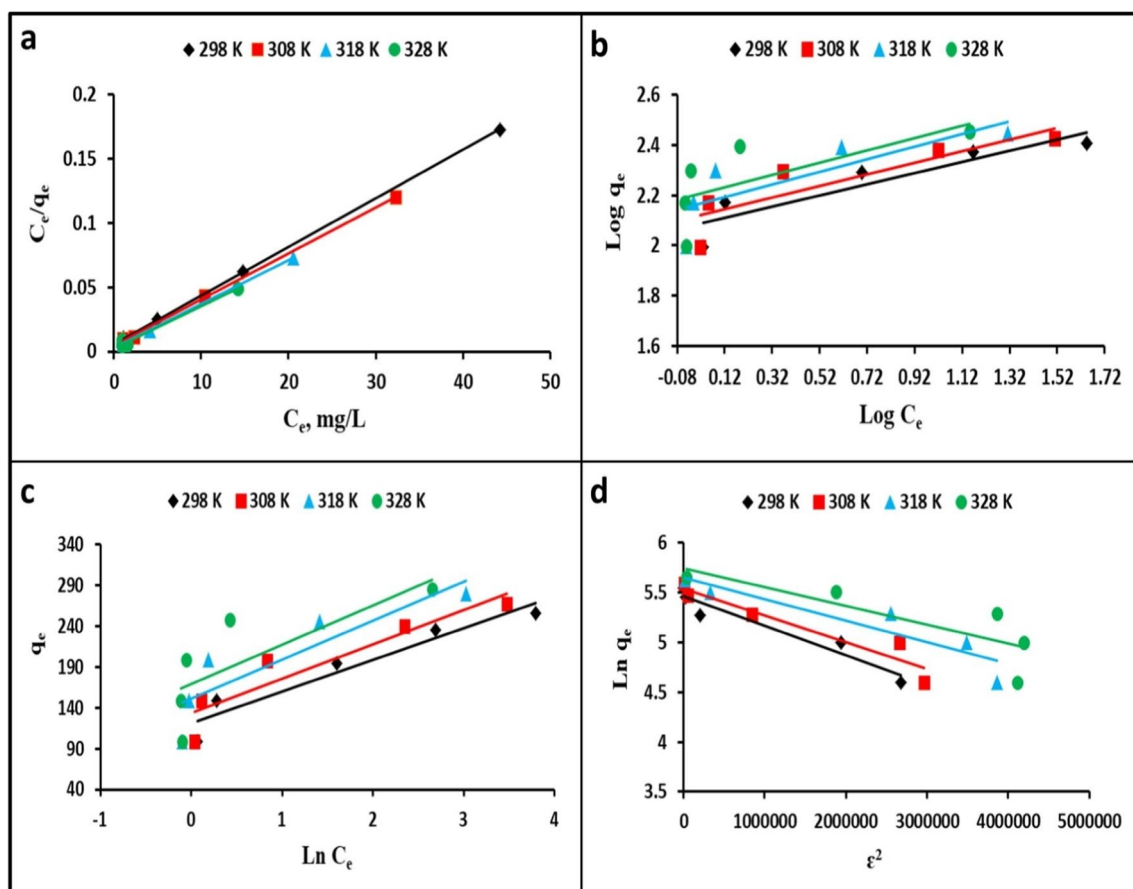

Fig. 8 Langmuir (**a**), Freundlich (**b**), Temikn (**c**), and D-R (**d**) linear plots of EY removal by CuS NPs–AC at temperatures 298, 308, 318, and 328 K

3.4.3 Temkin isotherm

Using the same experimental data, the Temkin isotherm model's applicability was also confirmed. Table 1 displays the constants identified using the Temkin plot (Fig. 8c). The Temkin isotherm's parameters were examined, and it became clear that the data did not accurately fit the model. The lower value of R^2 further supports its unsuitability (0.92, 0.87, 0.77, and 0.59 at 298, 308, 318, and 328 K, respectively). The high values of β for EY adsorption on CuS NPs–AC indicate a substantial ionic interaction between EY molecules and our adsorbent in the chosen temperature range (298–328 K).

3.4.4 Dubinin-Radushkevich isotherm

The validity of the D-R type isotherm was confirmed by analyzing the same experimental data used in this study. The parameters were established using the D-R plot, which is shown in Fig. 8d and Table 1. A detailed analysis at the D-R isotherm's parameters revealed that the data did not closely match the model. For this model, the R^2 values were lower (0.93, 0.91, 0.85, and 0.66 at 298, 308, 318, and 328 K, respectively). The magnitude of E works out to be 1.3–1.6 kJ/mol, suggesting that the physisorption phenomena played a significant part in the adsorption of EY dye onto CuS NPs–AC.

3.5 Kinetic analysis of adsorption

The chemical pathway and mechanism of adsorption are clarified by adsorption kinetics, which is a crucial component of understanding adsorption efficiency [85]. The experimental data was fitted using pseudo-first-order, pseudo-second-order, and Elovich models at room temperature (298 K) for different contact times and initial EY concentrations (200, 250, and 300 mg/L). The characteristics of each model are shown in Table 2. Pseudo-first-order kinetics assumes that the rate-limiting step in the adsorption process is the diffusion of the adsorbate to the surface of the adsorbent [43]. This assumption is based on the idea that the concentration of the adsorbate at the surface of the adsorbent is much lower than in the bulk solution [43]. Therefore, the rate of adsorption is directly proportional to the concentration of the adsorbate remaining in the solution. On the other hand, second-order kinetics assumes that the rate of adsorption is controlled by the chemical reaction between the adsorbate and the adsorbent. This type of adsorption is also known as chemisorption [79]. In this process, there is a transfer of electrons between the adsorbate and the adsorbent, leading to the formation of a chemical bond. The rate of adsorption in this case is directly proportional to the concentration of both the adsorbate and the adsorbent [79]. The pseudo-first-order

Table 2 Kinetic parameters of EY adsorption onto CuS NPs–AC under conditions: 0.1 g adsorbent over 200–300 mg/L at pH=7, contact time 10–120 min, and 298 K

Model	Parameter	Initial EY concentration (mg/L)		
		200	250	300
Pseudo-first order	K_1	0.047	0.049	0.056
	q_e (cal.)	92.51	221.56	659.48
	R^2	0.836	0.981	0.842
	SSE	0.297	0.034	1.78
	RMSE	0.222	0.07	0.472
	χ^2	0.049	0.005	0.222
Pseudo-second order	K_2	6e−4	3e−4	1e−4
	q_e (cal.)	212.77	277.78	370.37
	H	29.33	23.92	14.33
	R^2	0.999	0.999	0.991
	SSE	2.83×10^{-4}	1.81×10^{-4}	9.2×10^{-4}
	RMSE	0.222	0.07	0.472
	χ^2	2.83×10^{-5}	1.81×10^{-5}	9.2×10^{-5}
Elovich	β	0.032	0.02	0.013
	α	211.03	80.80	34.22
	R^2	0.939	0.960	0.973
	SSE	389.51	638.55	1020
	RMSE	6.24	7.99	10.1
	χ^2	38.95	63.85	102
Experimental adsorption capacity	q_e (exp.)	198.99	248.97	299.01

kinetic model is represented in the linear form (Eq. 10). The slope of the line produced by plotting log $(q_e - q_t)$ vs t was used to calculate the value of the rate constant (K_1) (Fig. 9a). The linear form for the pseudo-second-order model is represented by Eq. 11. The slope of the linear relationship between t/q and t, which can be seen when plotting the data (Fig. 9b), was used to determine the value of K_2. In comparison to the pseudo-first-order model, which had R^2 values between 0.950 and 0.985, R^2 of pseudo-second-order model was higher at all the investigated concentration and varied from 0.991 to 0.999. The q_e calculated from the pseudo-second-order model was quite similar to the value obtained experimentally. Overall, the predicted value was just slightly higher than the experimental value, supporting the validity of the pseudo-second-order model to evaluate the adsorption of EY by CuS NPs–AC. This result also suggests that the main mode of EY adsorption on CuS NPs–AC is chemical adsorption. The conclusions are in line with the results provided from the surface charge study and pH effect. These findings are consistent with previous researches on EY removal by xanthan-acacia hybrid super-adsorbent [3], carbon nanotube incorporated eucalyptus-derived activated carbon [4],
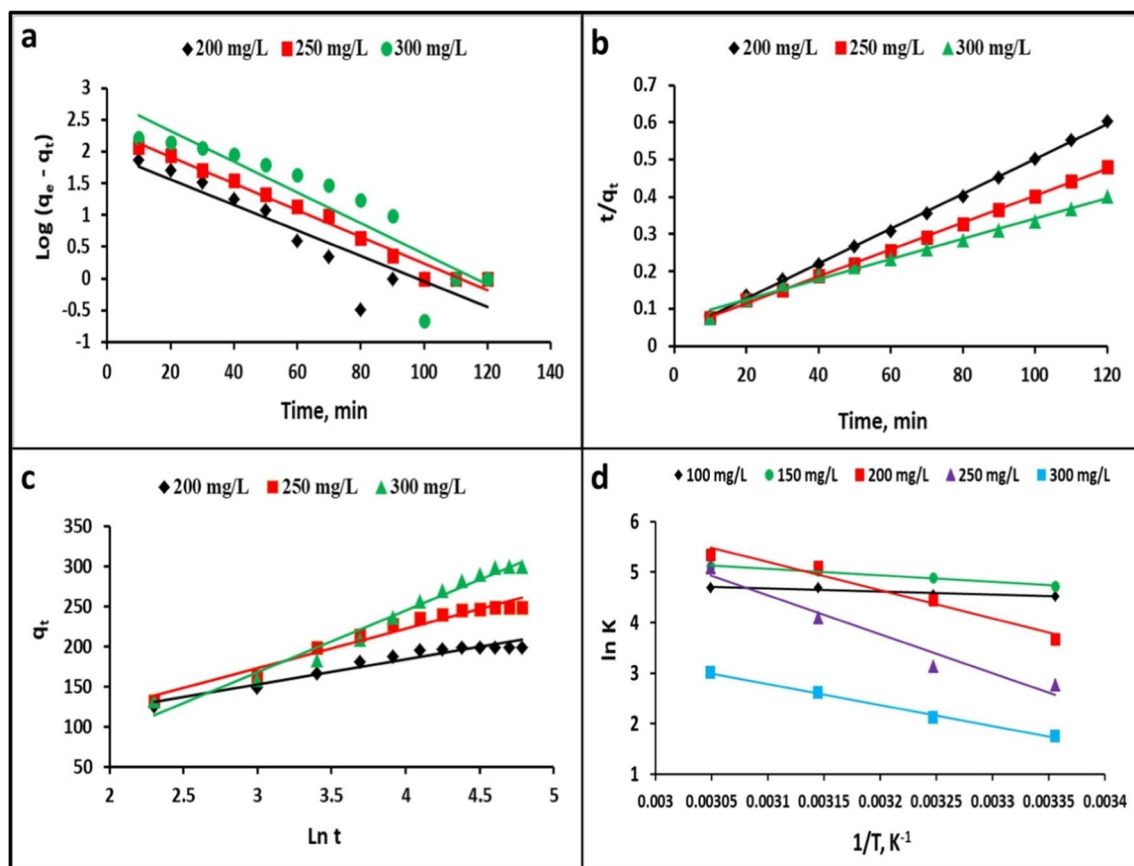
Fig. 9 Kinetic models of EY adsorption on CuS NPs–AC: (**a**) pseudo-first order, (**b**) pseudo-second order, (**c**) Elovich, and (**d**) plot of ln k versus 1/T for thermodynamic analysis

Co$_2$O$_3$-NP-AC [5], deep eutectic solvent functionalized CNT/ZnCo$_2$O$_4$ nanostructure [6], zinc oxide nanoparticles loaded on activated carbon prepared from walnut peel extract [51], lemon peel–based low-cost biosorbents [65], tri-metallic-layered double hydroxide nanosheets [67], clay/carbon composite [77], graphene oxide nanosheets and ZnO nanospheres [80], and iron sulfide–functionalized polyaniline nanocomposite [83]. Elovich equation (Eq. 12) has been commonly used for kinetic adsorption analyses. Table 2 presents the calculated values of α and β, which were obtained from the slope and intercept of the plot of adsorption capacity (q_t) against ln t shown in Fig. 9c. Furthermore, the plots showed strong linearity with the Elovich model, demonstrating that EY adsorption follows Elovich model in a comparable manner ($R^2 > 0.93$). Higher values of α calculated from the plot reveal faster adsorption kinetics occurred. Additionally, as shown in Table 2, the final values of α were greater than β for all initial dye concentration. In other words, it demonstrates that the rate of EY adsorption was greater than the rate of dye desorption. The chemisorption mechanism is generally supported by this kinetic model. It is revealed that the Elovich model's

results can explain that chemisorption is the dominant type of adsorption for EY by CuS NPs–AC [43].

3.6 Error functional analysis

Since measurement error affects the precision of the data, data samples from each experiment in a series of studies in the actual world differ from one another. Statistical error function is the method used to account for data errors in order to assure accurate measurement findings [50]. So, in order to assess the models' suitability, the isotherm and kinetic data were further examined using three error functions. Higher value of R^2 and lower values of SSE, $RMSE$, and χ^2 indicate the best fit of the model. The correlation of regression (R^2) and the error functions of the equilibrium data for EY adsorption (Table 1) suggest that the Langmuir isotherm model provides the best fit to the experimental data of EY adsorption onto CuS NPs–AC nanocomposite. In addition, the error functions and correlation of regression for the kinetic models (Table 2) reveal that EY adsorption onto CuS NPs–AC nanocomposite follows pseudo-second-order model. Thus, it was suggested

that the error functions and correlation of regression were appropriate and agreed with each other for validating isotherm and kinetic models.

3.7 Thermodynamic behavior of adsorption process

The Gibbs free energy ($\Delta G°$), enthalpy ($\Delta H°$), and entropy ($\Delta S°$) are crucial thermodynamic parameters in the adsorption process to assess the viability and spontaneous nature of the reaction. Equations 13–15 and van't Hoff equation were used to obtain the thermodynamic parameters. Figure 9d displays ln K_C vs $1/T$ fitted linear curve. At various temperatures, every negative $\Delta G°$ value points to a feasible and spontaneous process. In other words, a large negative value of $\Delta G°$ implies a stronger adsorption driving force, leading to an increase in adsorption capacity [43]. According to Table 3, the $\Delta G°$ value was found to be more negative at higher temperatures, indicating that EY was eliminated more spontaneously at higher temperatures. The negative values of $\Delta G°$ in this study for EY range from −4.27 to −14.95 kJ/mol indicating that physisorption is predominate in this system. The endothermic nature of the adsorption process is demonstrated by the positive $\Delta H°$ values of 5.2–64.02 kJ/mol. During the adsorption of EY dye on CuS NPs–AC, the positive values of $\Delta S°$ (0.055–0.13 kJ/mol.K) was also noted, suggesting greater randomness at the solid-liquid interface and the adsorption process of EY on CuS NPs–AC was stable and hard to desorb. Similar results were reported when nickel oxide nanoparticles [47], ferroferric oxide/polypyrrole magnetic composite [49], *Saccharomyces cerevisiae* biosorbent [72], teak leaf litter powder [73], and clay/carbon composite derived from spent bleaching earth [77] were employed for EY adsorption.

3.8 Practical applicability: interfering ions and selectivity

Practical wastewater has a complicated composition that typically includes inorganic salts and other materials. Ionic strength is a crucial factor in determining how well an adsorbent performs. The ideal CuS NPs–AC dosage is supplied to the simulated water to test the adsorbent's feasibility for real-time wastewater treatment. 100 mg/L of the regularly used dyeing ions NO_3^-, SO_4^{-2}, PO_4^{-3}, Cl^-, Mg^{2+}, Ca^{2+}, K^+, and Na^+ was added to the same concentration of EY dye solution to spike it. The removal percentage of EY does not markedly decreased (88.52±0.3% and 93.35±0.25% in the presence of anions and cations, respectively) by the adsorbent shows that the dye molecules have a strong affinity for the adsorbent sites (Fig. 10a and b).

Selectivity adsorption is a characteristic of high-quality adsorbents that facilitates the removal/recycling of particular adsorbates from complex sewage [86]. We examined the ability of CuS NPs–AC to selectively adsorb EY in three binary systems (EY/MB, EY/MG, and EY/CV). The complete experimental results are shown in Fig. 10c and Table 4. When EY solution and MB solution were combined at the same mass concentration, as seen in Fig. 10d, the resulting mixed solution displayed a dark violet color. The mixed solution appeared bright blue after being adsorbed by CuS NPs–AC, similar to the color of a single MB solution. This fact showed that CuS NPs–AC selectively adsorbed EY dye from EY/MB mixed solution. The binary mixed systems EY/MG and EY/CV also produced similar outcomes (Fig. 10d). Notably, the adsorption behavior of the three groups of mixed solutions varied slightly because the chemical structures of the cationic dyes MB, MG, and CV differed (see Fig. 10c). Other publications with similar findings can be found here [82, 87]. Therefore, we believe that CuS NPs–AC can be used as an effective adsorbent for separating out anionic dyes from cationic dye effluent.

3.9 Reusability of CuS NPs–AC adsorbent

Reusable adsorbents are essential for effective wastewater treatment. Evaluation of adsorbent reusability in real-world applications is essential for assessing long-term viability. In order to evaluate the reusability of CuS NPs–AC, a mixture of water and ethanol (1:1) was used as an eluent for desorption process at ambient temperature. The regenerated adsorbent was dried in an oven and

Table 3 Thermodynamic parameters for EY uptake by CuS NPs–AC

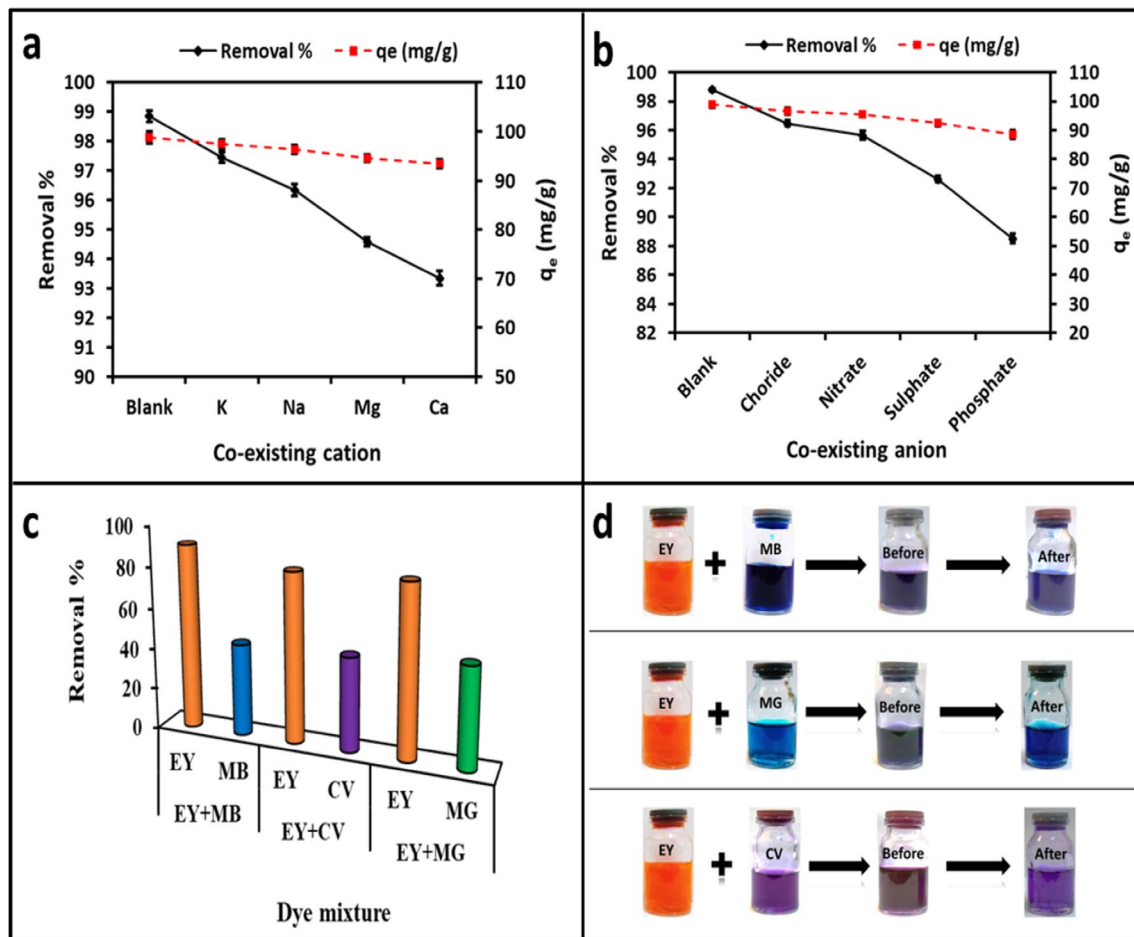| Parameter	Temp., K	Initial concentration, mg/L				
		100	150	200	250	300
$\Delta G°$ (kJ/mol)	**298**	−11.20	−11.73	−9.33	−6.35	−4.27
	308	−11.75	−12.49	−11.20	−8.72	−5.57
	318	−12.30	−13.25	−13.08	−11.08	−6.87
	328	−12.85	−14.00	−14.95	−13.44	−8.16
$\Delta H°$ (kJ/mol)		5.21	10.91	46.56	64.02	34.44
$\Delta S°$ (kJ/mol.K)		0.055	0.076	0.188	0.236	0.130

Fig. 10 Effect of coexisting cations (**a**) and anions (**b**), comparison of the adsorption percentage of EY&MB, EY&CV, and EY&MG (**c**), and (**d**) photographs of the binary mixtures before and after adsorption by CuS NPs–AC

Table 4 The effect of cationic dyes in a binary mixture on the adsorption of EY, removal percentage, and selectivity coefficients (α) using CuS NPs–AC

Binary mix.		Removal %	α
EY/MB	EY	**90.8**	**12.1**
	MB	**44.9**	
EY/CV	EY	**82.5**	**5.61**
	CV	**45.6**	
EY/MG	EY	**83.0**	**5.13**
	MG	**48.8**	

then used for five consecutive cycles under the following adsorption test (EY concentration of 300 mg/L, 2 g/L dose, 120 min contact time, and pH 7). The obtained results revealed that the as-prepared CuS NPs–AC can be reusable and recyclable without significant drop in its adsorption ability since the removal efficiency

and adsorption capacity were maintained higher ($89.45\pm0.05\%$, 268.27 ± 0.15 mg/g) even after five successive cycles (Fig. 11). Similar trend was also observed by [51] when using zinc oxide nanoparticles loaded on activated carbon for the effective removal of EY from aqueous solution. These authors reported a drop in the removal efficiency of EY from 93.44 to 81.74% after five recovery cycles. Thus, CuS NPs–AC is an economically viable adsorbent for wastewater treatment since it can be recycled multiple times before degrading.

3.10 Evaluation of the mechanism of EY adsorption onto CuS NPs–AC

The adsorption process of EY onto CuS NPs–AC can be further assessed by evaluating the adsorption mechanism. Adsorption may comprise several strategies, all of which may be influenced by various variables. Electrostatic attraction, π-π stacking, and surface complexation are examples
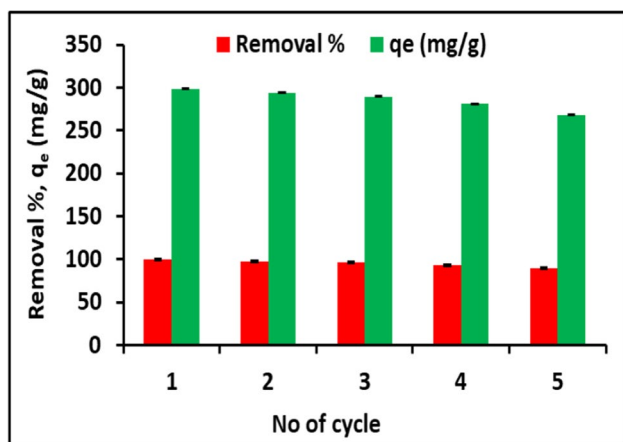
Fig. 11 Removal and adsorption capacity of EY after five cycles of reuse

$572 \ cm^{-1}$ were appeared in the FTIR spectrum, indicating that EY was successfully adsorbed on CuS NPs–AC. The absorption bands of the C–H stretching vibration at 2925 and $2858 \ cm^{-1}$ was increased, which might be caused by the C-H of EY molecules adsorbed on CuS NPs–AC. Compared with CuS NPs–AC, the characteristic absorption peaks around $3406 \ cm^{-1}$ (the stretching vibrations of OH and NH bonds) and $1397 \ cm^{-1}$ (the bending vibration of the O–H bond) was shifted and decreased, indicating that electrostatic interactions and hydrogen bonding were involved in the adsorption of EY dye [89]. The peak due to the stretching vibrations of C=C ($1617 \ cm^{-1}$) in CuS NPs–AC showed red shifts of $2 \ cm^{-1}$, which could be attributed to π-π and electrostatic interactions between CuS NPs–AC and EY [89]. In addition, the peaks of CuS at 677 and $596 \ cm^{-1}$ were diminished, confirming that CuS NPs may play an important role in EY adsorption process. Moreover, the comparison between elemental composition of CuS NPs–AC before and after adsorption process affirms its affinity for EY. Herein, EDX spectrum of CuS NPs–AC before adsorption of EY shows the presence of C (30.88%), O (29.28%), Si (0.1%), S (10.59%), Cu (25.42%), and Ca (3.71%) (Fig. 12c). After the adsorption of EY, the increase in C weight to 46.73%
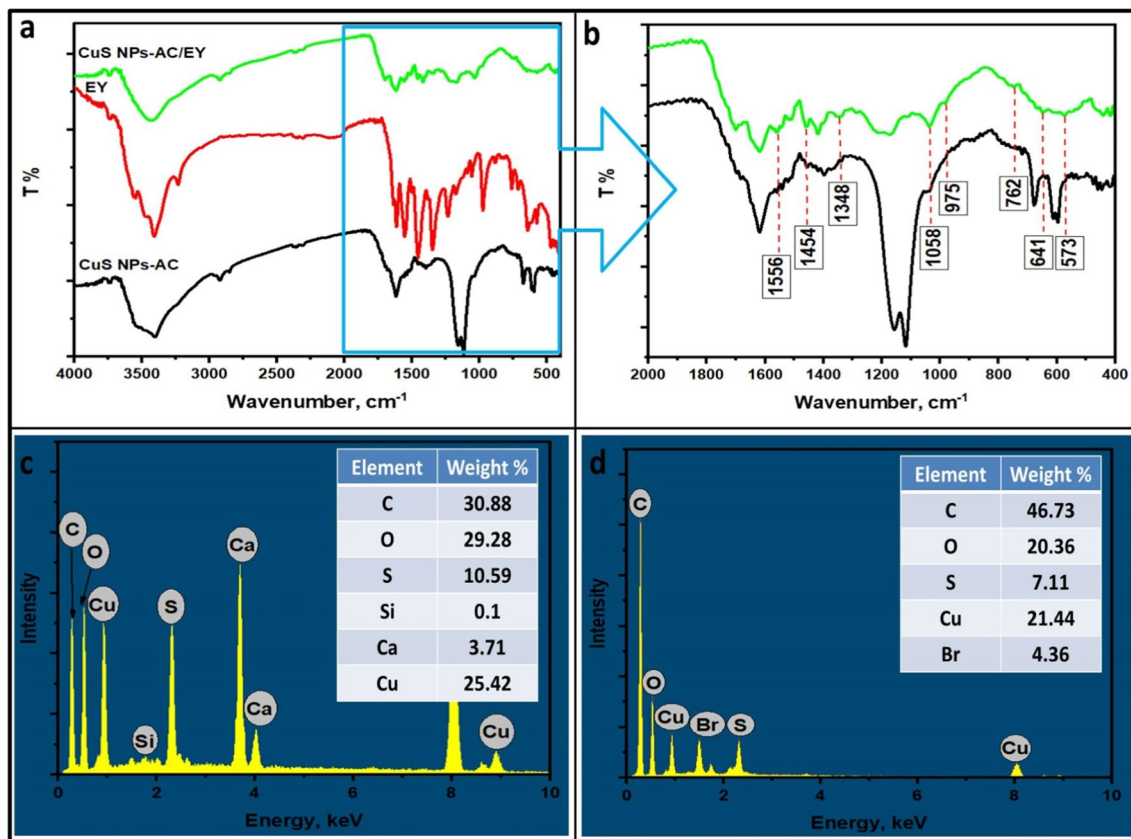
of potential adsorption mechanisms [88]. The adsorption mechanism was investigated by examining the FTIR spectra of CuS NPs–AC before and after EY adsorption (Fig. 12a and b). After adsorption, the characteristic weak absorption peaks of EY at 1556, 1454, 1348, 1058, 975, 762, 641, and

Fig. 12 FTIR spectra of CuS NPs–AC, EY, and CuS NPs–AC/EY (**a**), enlargement of the FTIR spectra of CuS NPs–AC and CuS NPs–AC/EY from 2000 to $400 \ cm^{-1}$ (**b**), and EDX profiles of CuS NPs–AC (**c**) and CuS NPs–AC/EY (**d**)

Table 5 Adsorption kinetic parameters of intraparticle diffusion model for EY adsorption onto CuS NPs–AC

Adsorbate	C_0 (mg/L)	K_{diff} [mg/g/(min)$^{1/2}$]			C (mg/g)		
		$K_{d,1}$	$K_{d,2}$	$K_{d,3}$	C_1	C_2	C_3
EY	200	17.79	7.52	0.13	68.89	134.84	197.61
	250	26.77	7.86	-	46.54	173.28	248.97
	300	24.05	22.09	0.23	53.70	82.55	296.54

may be attributed to EY sorption. This was also confirmed by the appearance of Br peaks in EDX spectrum of CuS NPs–AC after EY adsorption, as Br is one of the constituent elements of EY molecular structures. Nevertheless, some trace elements (calcium and silicon) seen in CuS NPs–AC unadsorbed species are completely absent in CuS NPs–AC before adsorption-loaded species (Fig. 12d). Additionally, Langmuir model, which is compatible with the adsorption process, was used to study the adsorption mechanism. CuS NPs–AC exceptional mesoporous structure may be responsible for its high monolayer adsorption capacity. The favorableness of adsorption process is predicted by the Langmuir parameter R_L. The fact that all R_L values fall between 0 and 1 indicates that the process is favorable. The negative values of $\Delta G°$ can similarly be used to verify this assertion. The computed values of $\Delta G°$ ('20 kJ/mol.) suggest that a physical adsorption mechanism may have an impact on the adsorption process. The $\Delta H°$ values (2–40 kJ/mol.) further indicate that hydrogen bond forces may be involved in the adsorption process [90]. The incorporation of kinetic models

to investigate experimental data on adsorption can serve in examining the mechanisms that govern the adsorption process, such as chemical reaction and diffusion control. The adsorption data were in good agreement with pseudo-second-order model, indicating that chemisorption may be the mechanism controlling EY adsorption. Functional groups on the adsorbent were used to chemically adsorb pollutants. By sharing electrons and constructing chemical bonds, CuS NPs–AC and EY dye may chemically interact through valency forces. The sorption process also typically entails the diffusion of adsorbate molecules to the boundary layer surrounding the adsorbent, followed by the diffusion of molecules from the boundary layer to the surface of the adsorbent and the internal membrane [91]. In order to explore the diffusion phenomenon during adsorption, the intraparticle diffusion model was adopted [91]. The equation below provides the initial rate of intraparticle diffusion:
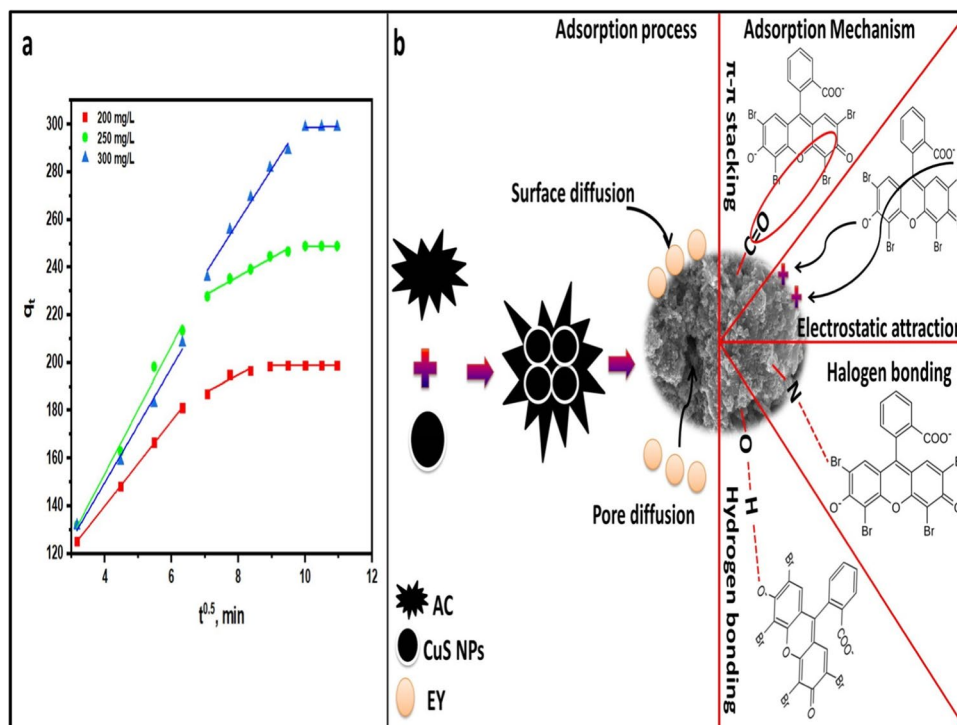
$$q_t = K_{id} * t^{0.5} + C \tag{19}$$

Fig. 13 Intra particle diffusion model of EY adsorption by CuS NPs–AC (**a**) and adsorption mechanism of EY onto CuS NPs–AC (**b**)

Table 6 Comparison of EY adsorption on various adsorbents

Adsorbent	pH	Dose (g/L)	Conc. (mg/L)	Time (min)	Temp (K)	q_{max} (mg/g)	Ref.
Xan-Aca-cl-poly(AAm)[a]	----	26.6	10-30	960	303	4.17	[3]
CNT/ZnCo$_2$O$_4$[b]	7	5	20-200	600	298	414.45	[6]
AC-ZnO[c]	3	1	100	30	----	163.9	[51]
Lemon peel	2	20	25	60	303	8.240	[65]
SBE/C[d]	----	1	20	----	298	11.15	[77]
TAC[e]	2	0.5	5-30	240	303	1.98	[81]
CAC[f]	2	0.5	5-30	240	303	3.13	[81]
GT[g]	2	0.5	25-300	240	303	27.78	[81]
COM[h]	2	0.5	25-300	240	303	30.30	[81]
PZS-PEI[i]	2	0.25	50-200	300	298	92.34	[82]
Chitosan/PVA[j]	6	2	10-50	40	298	52.91	[91]
GONS[k]	1	3	50	10	343	217.33	[92]
Cu (OH)$_2$ NPs-AC[l]	6	0.3	5	2.5	----	26.4	[93]
Fe$_3$O$_4$/PPy[m]	---	1	80-320	90	298	212.31	[49]
PC[n]	7	1	100-300	300	303	400	[94]
CuS NPs–AC	**7**	**2**	**100-300**	**120**	**328**	**303.03**	This study

[a]Xanthan-acacia hybrid cross-linked poly(acrylamide) chains

[b]Carbon nanotubes/ZnCo$_2$O$_4$ hybrid nanostructure

[c]Zinc oxide nanoparticles loaded on activated carbon

[d]Clay/carbon composite derived from spent bleaching earth

[e]Thermally activated charcoal derived from date palm seeds

[f]Chemically activated charcoal derived from date palm seeds

[g]Goethite

[h]Composite of goethite/thermally activated charcoal derived from date palm seeds

[i]Polyethyleneimine-grafted polyphosphazene microspheres

[j]Nano-sized chitosan-blended polyvinyl alcohol

[k]Graphene oxide nanosheets

[l]Cu (OH)$_2$ nanoparticle–loaded activated carbon

[m]Ferroferric oxide/polypyrrole magnetic composite

[n]Porous carbon prepared from tea waste

where q_t is the amount of dye on the surface of the sorbent at time t (mg/g), K_{id} is the intraparticle diffusion rate constant (mg/g. min$^{0.5}$), t is the time (min), and C is the intercept which denotes the thickness of the boundary layer (mg/g). The computed adsorption kinetic parameters are shown in Table 5. The fact that the intercept (C) of the fitted equation was not zero (Fig. 13a and Table 5) suggests that there are several adsorption mechanisms controlling the sorption rate. Three stages of kinetics data fitting were distinguished: Due to the large number of active sites on the adsorbent's surface, the first stage shows how EY quickly undergoes surface diffusion [82]. The second stage involves gradual adsorption, which is caused by EY's continued diffusion within CuS NPs–AC. The line's slope does, however, decline from the first step, and the adsorption rate essentially flattens out [82]. This event supports the kinetics analysis by demonstrating

that the adsorption process was primarily constrained by surface diffusion (chemisorption). The third step is known as the adsorption equilibrium stage, during which the adsorption process gradually slows down as the concentration of EY in the solution decreases [6]. The bigger boundary layer effect is correlated with a higher C value, which increases the likelihood of external mass transfer and decreases the likelihood of internal mass transfer [6]. CuS NPs–AC possesses a mesoporous structure, which may be the cause of its comparatively thick boundary layer. Therefore, it is impossible to disregard how the thickness of the boundary layer affects adsorption. In conclusion, π-π stacking, electrostatic attraction, halogen bonding, and hydrogen bonding are primarily responsible for strong EY adsorption ability of CuS NPs–AC (Fig. 13b).

3.11 Comparison with other adsorbents

The maximum sorption capacity of the environmentally benign prepared CuS NPs–AC nanocomposite was compared with other adsorbents as mentioned in the literature in order to validate its supremacy for the adsorption of EY in an aqueous environment. Table 6 demonstrates that the CuS NPs–AC nanocomposite is a superior EY adsorbent compared to many others [3, 6, 49, 51, 65, 77, 81, 82, 91–94]. The finding may be related to the surface functionalization of AC by CuS NPs, which introduces a significant number of active sites for EY adsorption. Due to the abundance of hydrophilic groups including hydroxyl, amine, and carboxylic groups on its surface, CuS NPs–AC nanocomposite can disperse efficiently in water. CuS NPs–AC nanocomposite is the excellent adsorbent because it has a large surface area and abundant hydrophilic groups. Additionally, a substantial part of the higher adsorption process by electrostatic interaction is played by the existence of C=O, C-O-C, and/or O-C=O groups, which are linked to the abundance of potential binding sites in carbon-based nanocomposite. A key aspect towards widespread and sustainability is the large-scale fabrication of economical, high-quality AC nanocomposites from algal biomass using environmentally friendly processes. As a result, the suggested synthetic method in this study is affordable, straightforward, quick, and calls for reasonable conditions. In addition, CuS NPs were also produced by cost-effective green method using algal extract. This is a simple, stable, environmentally friendly, affordable, and cost-effective biological process that could boost industrial production. In this study, we investigated an economical method for the production of CuS NPs–AC nanocomposite. The positive outcomes could open up a wide range of opportunities for additional organic contaminants.

4 Conclusions

In this work, simple, low-cost, and eco-friendly adsorbent based on porous activated carbon derived from *SS* alga as a biomass precursor and biosynthesized CuS NPs was successfully prepared and characterized via FTIR, XRD, SEM-EDX, BET, and BJH. The newly synthesized CuS NPs–AC was evaluated for EY dye adsorption from aqueous solutions. The results of all experiments in this work demonstrate that the obtained CuS NPs–AC functions as a potent adsorbent to remove EY from wastewater. Based on the equilibrium adsorption data, it was observed that the adsorption process followed Langmuir isotherm at all temperatures with maximum monolayer adsorption capacity of 303.03 mg/g at 328 K. Furthermore, the adsorption process exhibited a pseudo-second-order kinetics, regardless of the initial dye concentration. In this study, it was found that the adsorption processes were feasible, spontaneous, and endothermic at all tested temperatures as indicated by the calculated thermodynamic parameters. Mechanism of EY adsorption onto CuS NPs–AC showed the involvement of H-bonding, electrostatic interaction, intraparticle diffusion, and π-π stacking. These findings suggest that the prepared CuS NPs–AC could be a promising alternative to commercial AC for wastewater treatment.

Declarations

References

1. Pandey S (2017) A comprehensive review on recent developments in bentonite-based materials used as adsorbents for wastewater treatment. J Mol Liq 241:1091–1113
2. Pandey S, Ramontja J (2016) Natural bentonite clay and its composites for dye removal: current state and future potential. Am J Chem Appl 3(2):8–19
3. Sharma AK, Kaith BS, Bajaj S, Bhatia JK, Panchal S, Sharma N, Tanwar V (2019) Efficient capture of eosin yellow and crystal violet with high performance xanthan-acacia hybrid super-adsorbent optimized using response surface methodology. Colloids Surf B Biointerfaces 175:314–323
4. Yadav SK, Dhakate SR, Singh BP (2022) Carbon nanotube incorporated eucalyptus derived activated carbon-based novel adsorbent for efficient removal of methylene blue and eosin yellow dyes. Bioresour Technol 344:126231

5. Assefi P, Ghaedi M, Ansari A, Habibi MH, Momeni MS (2014) Artificial neural network optimization for removal of hazardous dye Eosin Y from aqueous solution using Co_2O_3-NP-AC: Isotherm and kinetics study. J Ind Eng Chem 20(5):2905–2913

6. Lawal IA, Dolla TH, Pruessner K, Ndungu P (2019) Synthesis and characterization of deep eutectic solvent functionalized $CNT/ZnCo_2O_4$ nanostructure: kinetics, isotherm and regenerative studies on Eosin Y adsorption. J Environ Chem Eng 7(1):102877

7. Fadillah G, Saleh TA, Wahyuningsih S, Putri ENK, Febrianastuti S (2019) Electrochemical removal of methylene blue using alginate-modified graphene adsorbents. Chem Eng J 378:122140

8. Zhijiang C, Ping X, Cong Z, Tingting Z, Jie G, Kongyin Z (2018) Preparation and characterization of a bi-layered nano-filtration membrane from a chitosan hydrogel and bacterial cellulose nanofiber for dye removal. Cellulose 25(9):5123–5137

9. Othmani A, Kesraoui A, Seffen M (2017) The alternating and direct current effect on the elimination of cationic and anionic dye from aqueous solutions by electrocoagulation and coagulation flocculation. Euro-Mediterr J Environ Integr 2(1):1–12

10. Vieira IRS, da Silva AA, da Silva BD, Neto LT, Tessaro L, Furtado CRG, Conte-Junior CA (2023) Eco-friendly synthesis of ZnO nanomaterial from green tea extract: photocatalytic, antibacterial and antioxidant potential. Biomass Convers Biorefin:1–15

11. Patel HK, Kalaria RK, Jokhakar PH, Patel CR, Patel BY (2022) Removal of emerging contaminants in water treatment by an application of nanofiltration and reverse osmosis. In: Development in wastewater treatment research and processes. Elsevier, pp 385–400

12. El Messaoudi N, El Khomri M, El Mouden A, Bouich A, Jada A, Lacherai A, Américo-Pinheiro JHP (2022) Regeneration and reusability of non-conventional low-cost adsorbents to remove dyes from wastewaters in multiple consecutive adsorption–desorption cycles: a review. Biomass Convers Biorefin:1–18

13. Hasan IMA, Salman HMA, Hafez OM (2022b, 2022) Ficus-mediated green synthesis of manganese oxide nanoparticles for adsorptive removal of malachite green from aqueous solutions. Environ Sci Pollut Res

14. Pandey S, Son N, Kang M (2022) Synergistic sorption performance of karaya gum crosslink poly (acrylamide-co-acrylonitrile)@ metal nanoparticle for organic pollutants. Int J Biol Macromol 210:300–314

15. Pandey S, Son N, Kim S, Balakrishnan D, Kang M (2022) Locust bean gum-based hydrogels embedded magnetic iron oxide nanoparticles nanocomposite: advanced materials for environmental and energy applications. Environ Res 214:114000

16. Tandekar SA, Pande MA, Shekhawat A, Fosso-Kankeu E, Pandey S, Jugade RM (2022) Fe (III)–chitosan microbeads for adsorptive removal of Cr (VI) and phosphate ions. Minerals 12(7):874

17. Doondani P, Jugade R, Gomase V, Shekhawat A, Bambal A, Pandey S (2022) Chitosan/graphite/polyvinyl alcohol magnetic hydrogel microspheres for decontamination of reactive orange 16 dye. Water 14(21):3411

18. Manyà JJ, González B, Azuara M, Arner G (2018) Ultramicroporous adsorbents prepared from vine shoots-derived biochar with high CO_2 uptake and CO_2/N_2 selectivity. Chem Eng J 345:631–639

19. Idrees M, Rangari V, Jeelani S (2018) Sustainable packaging waste-derived activated carbon for carbon dioxide capture. J CO2 Util 26:380–387

20. Serafin J, Baca M, Biegun M, Mijowska E, Kaleńczuk RJ, Sreńscek-Nazzal J, Michalkiewicz B (2019) Direct conversion of biomass to nanoporous activated biocarbons for high CO_2 adsorption and supercapacitor applications. Appl Surf Sci 497:143722

21. Abuelnoor N, AlHajaj A, Khaleel M, Vega LF, Abu-Zahra MR (2021) Activated carbons from biomass-based sources for CO_2 capture applications. Chemosphere 282:131111

22. Hou ZQ, Luo MY, Yang YT, Zhou JC, Liu LC, Cai JJ (2021) Algae-based carbons: design, preparation and recent advances in their use in energy storage, catalysis and adsorption. New Carbon Mater 36(2):278–303

23. Elayappan T, Jayanarayanan B, Daniel AP (2022) Production of biochar from Keppaphycus alvarezii (macroalgae) for the removal of eosin yellow: desorption, kinetic, and isotherm studies. Biomass Convers Biorefin:1–12

24. Devault DA, Pierre R, Marfaing H, Dolique F, Lopez PJ (2021) Sargassum contamination and consequences for downstream uses: a review. J Appl Phycol 33(1):567–602

25. Barquilh CER, Cossich ES, Tavares CRG, Silva EA (2019) Biosorption of nickel (II) and copper (II) ions by Sargassum sp. in nature and alginate extraction products. Bioresour Technol Rep 5:43–50

26. de Souza Coracao AC, Dos Santos FC, Duarte JAD, Lopes-Filho EAP, De-Paula JC, Rocha LM, Teixeira VL (2020) What do we know about the utilization of the Sargassum species as biosorbents of trace metals in Brazil? J Environ Chem Eng 8(4):103941

27. Francoeur M, Ferino-Pérez A, Yacou C, Jean-Marius C, Emmanuel E, Chérémond Y, Gaspard S (2021) Activated carbon synthetized from Sargassum (sp) for adsorption of caffeine: Understanding the adsorption mechanism using molecular modeling. J Environ Chem Eng 9(1):104795

28. Pandey S, Makhado E, Kim S, Kang M (2022) Recent developments of polysaccharide based superabsorbent nanocomposite for organic dye contamination removal from wastewater—a review. Environ Res:114909

29. Kumar N, Gusain R, Pandey S, Ray SS (2023) Hydrogel nanocomposite adsorbents and photocatalysts for sustainable water purification. Adv Mater Interfaces 10(2):2201375

30. Mokhtari P, Ghaedi M, Dashtian K, Rahimi MR, Purkait MK (2016) Removal of methyl orange by copper sulfide nanoparticles loaded activated carbon: kinetic and isotherm investigation. J Mol Liq 219:299–305

31. Sharifpour E, Khafri HZ, Ghaedi M, Asfaram A, Jannesar R (2018) Isotherms and kinetic study of ultrasound-assisted adsorption of malachite green and Pb^{2+} ions from aqueous samples by copper sulfide nanorods loaded on activated carbon: experimental design optimization. Ultrason Sonochem 40:373–382

32. Dastkhoon M, Ghaedi M, Asfaram A, Javadian H (2018) Synthesis of CuS nanoparticles loaded on activated carbon composite for ultrasound-assisted adsorption removal of dye pollutants: process optimization using CCD/RSM, equilibrium and kinetic studies. Appl Organomet Chem 32(5):e4350

33. Borah D, Saikia P, Sarmah P, Gogoi D, Rout J, Ghosh NN, Bhattacharjee CR (2022) Composition controllable alga-mediated green synthesis of covellite CuS nanostructure: an efficient photocatalyst for degradation of toxic dye. Inorg Chem Commun 142:109608

34. Pejjai B, Reddivari M, Kotte TRR (2020) Phase controllable synthesis of CuS nanoparticles by chemical co-precipitation method: effect of copper precursors on the properties of CuS. Mater Chem Phys 239:122030

35. Nafees M, Ali S, Idrees S, Rashid K, Shafique MA (2013) A simple microwave assists aqueous route to synthesis CuS nanoparticles and further aggregation to spherical shape. Appl Nanosci 3:119–124

36. Krishnamoorthy K, Veerasubramani GK, Radhakrishnan S, Kim SJ (2015) Preparation of copper sulfide nanoparticles by sonochemical method and study on their electrochemical properties. J Nanosci Nanotechnol 15(6):4409–4413

37. Krishnamoorthy K, Veerasubramani GK, Rao AN, Kim SJ (2014) One-pot hydrothermal synthesis, characterization and

electrochemical properties of CuS nanoparticles towards supercapacitor applications. Mater Res Express 1(3):035006

38. Zhong R, Peng C, Chen L, Yu N, Liu Z, Zhu M, Chen Z (2016) Egg white-mediated green synthesis of CuS quantum dots as a biocompatible and efficient 980 nm laser-driven photothermal agent. RSC Adv 6(46):40480–40488

39. Zhou NQ, Tian LJ, Wang YC, Li DB, Li PP, Zhang X, Yu HQ (2016) Extracellular biosynthesis of copper sulfide nanoparticles by Shewanella oneidensis MR-1 as a photothermal agent. Enzym Microb Technol 95:230–235

40. Schaffie M, Hosseini MR (2014) Biological process for synthesis of semiconductor copper sulfide nanoparticle from mine wastewaters. J Environ Chem Eng 2(1):386–391

41. Xiong Y, Sun F, Zhang Y, Yang Z, Liu P, Zou Y, Xu Z (2019) Polydopamine-mediated bio-inspired synthesis of copper sulfide nanoparticles for T1-weighted magnetic resonance imaging guided photothermal cancer therapy. Colloids Surf B Biointerfaces 173:607–615

42. Hosseini MR, Schaffie M, Pazouki M, Darezereshki E, Ranjbar M (2012) Biologically synthesized copper sulfide nanoparticles: production and characterization. Mater Sci Semicond Process 15(2):222–225

43. Hasan IM, Tawfik AR, Assaf FH (2023) A novel Sargassum siliquastrum-stabilized MnS nanospheres for malachite green adsorption from aqueous solutions. Sep Sci Technol 58(5):893–915

44. Chaudhary R, Nawaz K, Khan AK, Hano C, Abbasi BH, Anjum S (2020) An overview of the algae-mediated biosynthesis of nanoparticles and their biomedical applications. Biomolecules 10(11):1498

45. Esmaeili A, Ghasemi S, Sohrabipour J (2010) Biosorption of copper from wastewater by activated carbon preparation from alga Sargassum sp. Nat Prod Res 24(4):341–348

46. Jain SN, Tamboli SR, Sutar DS, Marathe JV, Mawal VN (2022) Kinetic, equilibrium, thermodynamic, and desorption studies for sequestration of acid dye using waste biomass as sustainable adsorbents. Biomass Convers Biorefinery 12(7):2597–2609

47. Mahmood USB, Eisa MY, Hammed AK (2021) Adsorption of the eosin yellow dye by nickel oxide nanoparticles catalyzes via oxalate co-precipitation method: isotherm, kinetic and thermodynamic studies. Phys Scr 96(12):124056

48. Bai MT, Anudeep YV, Raju CA, Rao PV, Chittibabu N (2021) Decolourization of Eosin yellow (EY) dye using a variety of brown algae. Mater Today: Proc 42:1130–1137

49. Zhang M, Yu Z, Yu H (2020) Adsorption of Eosin Y, methyl orange and brilliant green from aqueous solution using ferroferric oxide/polypyrrole magnetic composite. Polym Bull 77(2):1049–1066

50. Rahman MS, Sathasivam KV (2015) Heavy metal adsorption onto Kappaphycus sp. from aqueous solutions: the use of error functions for validation of isotherm and kinetics models. Biomed Res Int 2015

51. Rashtbari Y, Afshin S, Hamzezadeh A, Gholizadeh A, Ansari FJ, Poureshgh Y, Fazlzadeh M (2022) Green synthesis of zinc oxide nanoparticles loaded on activated carbon prepared from walnut peel extract for the removal of Eosin Y and Erythrosine B dyes from aqueous solution: experimental approaches, kinetics models, and thermodynamic studies. Environ Sci Pollut Res 29(4):5194–5206

52. Yamil LDO, Georgin J, Franco DS, Netto MS, Piccilli DG, Foletto EL, Dotto GL (2021) High-performance removal of 2, 4-dichlorophenoxyacetic acid herbicide in water using activated carbon derived from Queen palm fruit endocarp (Syagrus romanzoffiana). J Environ Chem Eng 9(1):104911

53. Georgin J, Franco D, Drumm FC, Grassi P, Netto MS, Allasia D, Dotto GL (2020) Powdered biosorbent from the mandacaru cactus (Cereus jamacaru) for discontinuous and continuous

removal of Basic Fuchsin from aqueous solutions. Powder Technol 364:584–592

54. Georgin J, Yamil LDO, Franco DS, Netto MS, Piccilli DG, Perondi D, Dotto GL (2021) Development of highly porous activated carbon from Jacaranda mimosifolia seed pods for remarkable removal of aqueous-phase ketoprofen. J Environ Chem Eng 9(4):105676

55. Lima DR, Hosseini-Bandegharaei A, Thue PS, Lima EC, de Albuquerque YR, dos Reis GS, Tran HN (2019) Efficient acetaminophen removal from water and hospital effluents treatment by activated carbons derived from Brazil nutshells. Colloids Surf A Physicochem Eng Asp 583:123966

56. Cunha MR, Lima EC, Lima DR, da Silva RS, Thue PS, Seliem MK, Larsson SH (2020) Removal of captopril pharmaceutical from synthetic pharmaceutical-industry wastewaters: use of activated carbon derived from Butia catarinensis. J Environ Chem Eng 8(6):104506

57. Thue PS, Umpierres CS, Lima EC, Lima DR, Machado FM, Dos Reis GS, Tran HN (2020) Single-step pyrolysis for producing magnetic activated carbon from tucumã (Astrocaryum aculeatum) seed and nickel (II) chloride and zinc (II) chloride. Application for removal of nicotinamide and propanolol. J Hazard Mater 398:122903

58. Lima DR, Lima EC, Thue PS, Dias SL, Machado FM, Seliem MK, Rinklebe J (2021) Comparison of acidic leaching using a conventional and ultrasound-assisted method for preparation of magnetic-activated biochar. J Environ Chem Eng 9(5):105865

59. Saranya M, Ramachandran R, Samuel EJJ, Jeong SK, Grace AN (2015) Enhanced visible light photocatalytic reduction of organic pollutant and electrochemical properties of CuS catalyst. Powder Technol 279:209–220

60. Yang C, Jiang C, Fu Y, Chen F, Hu J (2022) Fast and effective uptake of mercury (II) from aqueous solution using waste carbon black-supported CuS composites and reutilization of spent adsorbent for photodegradation of rhodamine B. J Mol Liq 345:118251

61. Guo F, Zhan Y, Jia X, Zhou H, Liang S, Qian L (2021) Fabrication of nitrogen-doped hierarchical porous carbons from Sargassum as advanced electrode materials for supercapacitors. New J Chem 45(34):15514–15524

62. Franco DS, Georgin J, Netto MS, Allasia D, Oliveira ML, Foletto EL, Dotto GL (2021) Highly effective adsorption of synthetic phenol effluent by a novel activated carbon prepared from fruit wastes of the Ceiba speciosa forest species. J Environ Chem Eng 9(5):105927

63. Li C, He P, Jia L, Zhang X, Zhang T, Dong F, Liu H (2019) Facile synthesis of 3D CuS micro-flowers grown on porous activated carbon derived from pomelo peel as electrode for high-performance supercapacitors. Electrochim Acta 299:253–261

64. Ighalo JO, Adeniyi AG (2020) A mini-review of the morphological properties of biosorbents derived from plant leaves. SN Appl Sci 2(3):1–16

65. Bukhari A, Ijaz I, Zain H, Gilani E, Nazir A, Bukhari A, Iram S (2022) Removal of Eosin dye from simulated media onto lemon peel-based low cost biosorbent. Arab J Chem 15(7):103873

66. Divya P, Prithiba A, Rajalakshmi R (2019) Biomass derived functional carbon from Sargassum Wightii seaweed for supercapacitors. In: IOP Conference Series: Materials Science and Engineering (561, 1, 012078). IOP Publishing.

67. Nazir MA, Najam T, Bashir MS, Javed MS, Bashir MA, Imran M, Shah SSA (2022) Kinetics, isothermal and mechanistic insight into the adsorption of eosin yellow and malachite green from water via tri-metallic layered double hydroxide nanosheets. Korean J Chem Eng 39(1):216–226

68. Lee SM, Lee SH, Jung DH (2021) Surface oxidation of petroleum pitch to improve mesopore ratio and specific surface area of activated carbon. Sci Rep 11(1):1–9

69. Alamin NU, Khan AS, Nasrullah A, Iqbal J, Ullah Z, Din IU, Khan SZ (2021) Activated carbon-alginate beads impregnated with surfactant as sustainable adsorbent for efficient removal of methylene blue. Int J Biol Macromol 176:233–243

70. Mani SK, Bhandari R (2022) Microwave-assisted synthesis of self-assembled network of graphene oxide-polyethylenimine-polyvinyl alcohol hydrogel beads for removal of cationic and anionic dyes from wastewater. J Mol Liq 345:117809

71. Rehman TU, Bibi S, Khan M, Ali I, Shah LA, Khan A, Ateeq M (2019) Fabrication of stable superabsorbent hydrogels for successful removal of crystal violet from waste water. RSC Adv 9(68):40051–40061

72. Bahramifar N, Tavasolli M, Younesi H (2015) Removal of eosin Y and eosin B dyes from polluted water through biosorption using Saccharomyces cerevisiae: isotherm, kinetic and thermodynamic studies. J Appl Res Water Wastewater 2(1):108–114

73. Oyelude EO, Awudza JA, Twumasi SK (2017) Equilibrium, kinetic and thermodynamic study of removal of eosin yellow from aqueous solution using teak leaf litter powder. Sci Rep 7(1):1–10

74. Yao G, Bi W, Liu H (2020) pH-responsive magnetic graphene oxide/poly (NVI-co-AA) hydrogel as an easily recyclable adsorbent for cationic and anionic dyes. Colloids Surf A Physicochem Eng Asp 588:124393

75. Vo TS, Vo TTBC, Suk JW, Kim K (2020) Recycling performance of graphene oxide-chitosan hybrid hydrogels for removal of cationic and anionic dyes. Nano Converg 7(1):1–11

76. Wong S, Ghafar NA, Ngadi N, Razmi FA, Inuwa IM, Mat R, Amin NAS (2020) Effective removal of anionic textile dyes using adsorbent synthesized from coffee waste. Sci Rep 10(1):1–13

77. Liu Y, Chen Y, Shi Y, Wan D, Chen J, Xiao S (2021) Adsorption of toxic dye Eosin Y from aqueous solution by clay/carbon composite derived from spent bleaching earth. Water Environ Res 93(1):159–169

78. Chang Z, Chen Y, Tang S, Yang J, Chen Y, Chen S, Yang Z (2020) Construction of chitosan/polyacrylate/graphene oxide composite physical hydrogel by semi-dissolution/acidification/sol-gel transition method and its simultaneous cationic and anionic dye adsorption properties. Carbohydr Polym 229:115431

79. Shrestha D (2021) Removal of eosin Y dye using activated carbons from modified wood dust powder of Dalbergia sisoo. Patan Pragya 8(01):57–72

80. Ahmad N, Karim S, Hussain D, Mok YS, Siddiqui GU (2022) Efficient dual adsorption of eosin Y and methylene blue from aqueous solution using nanocomposite of graphene oxide nanosheets and ZnO nanospheres. Korean J Chem Eng 39(11):3155–3164

81. Abdus-Salam N, Ikudayisi-Ugbe AV, Ugbe FA (2021) Adsorption studies of acid dye–Eosin yellow on date palm seeds, goethite and their composite. Chem Data Collect 31:100626

82. Yu S, Feng M, Wu P, Liu H, Liu S, Fu J (2021) Polyethyleneimine-grafted polyphosphazene microspheres for rapid and efficient capture of anionic dyes from wastewater. Materials Today Chemistry 21:100525

83. Danu BY, Agorku ES, Ampong FK, Awudza JAM, Torve V, Danquah IMK, Ray SS (2021) Iron sulfide functionalized polyaniline nanocomposite for the removal of eosin Y from water: equilibrium and kinetic studies. Polym Sci Ser B 63(3):304–313

84. Giri BS, Sonwani RK, Varjani S, Chaurasia D, Varadavenkatesan T, Chaturvedi P, Pandey A (2022) Highly efficient bio-adsorption of Malachite green using Chinese Fan-Palm Biochar (Livistona chinensis). Chemosphere 287:132282

85. Baytar O, Ceyhan AA, Şahin Ö (2021) Production of activated carbon from Elaeagnus angustifolia seeds using H_3PO_4 activator and methylene blue and malachite green adsorption. Int J Phytoremediation 23(7):693–703

86. Belcaid A, Beakou BH, Bouhsina S, Anouar A (2022) Insight into adsorptive removal of methylene blue, malachite green, and rhodamine B dyes by cassava peel biochar (Manihot esculenta Crantz) in single, binary, and ternary systems: competitive adsorption study and theoretical calculations. Biomass Convers Biorefinery:1–24

87. Isik Z, Saleh M, M'barek I, Yabalak E, Dizge N, Deepanraj B (2022) Investigation of the adsorption performance of cationic and anionic dyes using hydrochared waste human hair. Biomass Convers Biorefinery:1–14

88. Hokkanen S, Bhatnagar A, Sillanpää M (2016) A review on modification methods to cellulose-based adsorbents to improve adsorption capacity. Water Res 91:156–173

89. Huang F, Tian X, Wei W, Xu X, Li J, Guo Y, Zhou Z (2022) Wheat straw-core hydrogel spheres with polypyrrole nanotubes for the removal of organic dyes. J Clean Prod 344:131100

90. Ghasemi M, Mashhadi S, Asif M, Tyagi I, Agarwal S, Gupta VK (2016) Microwave-assisted synthesis of tetraethylenepentamine functionalized activated carbon with high adsorption capacity for Malachite green dye. J Mol Liq 213:317–325

91. Anitha T (2016) Synthesis of nano-sized chitosan blended polyvinyl alcohol for the removal of Eosin Yellow dye from aqueous solution. J Water Process Eng 13:127–136

92. Veerakumar P, Tharini J, Ramakrishnan M, Panneer Muthuselvam I, Lin KC (2017) Graphene oxide nanosheets as an efficient and reusable sorbents for eosin yellow dye removal from aqueous solutions. ChemistrySelect 2(13):3598–3607

93. Dashamiri S, Ghaedi M, Asfaram A, Zare F, Wang S (2017) Multi-response optimization of ultrasound assisted competitive adsorption of dyes onto Cu $(OH)_2$-nanoparticle loaded activated carbon: central composite design. Ultrason Sonochem 34:343–353

94. Borah L, Goswami M, Phukan P (2015) Adsorption of methylene blue and eosin yellow using porous carbon prepared from tea waste: adsorption equilibrium, kinetics and thermodynamics study. J Environ Chem Eng 3(2):1018–1028

Publisher's Note Springer Nature remains neutral with regard to jurisdictional claims in published maps and institutional affiliations.